Debris Flow Impact on Rigid Vertical Barrier Wall, under the Protection by Tree Trunk Patches: Numerical and Analytical Modelling

Pakhshan Ahmadian

Submitted to the
Institute of Graduate Studies and Research
in partial fulfillment of the requirements for the degree of

Doctor of Philosophy
of
Civil Engineering

Eastern Mediterranean University
September 2024
Gazimağusa, North Cyprus

Approval of the Institute of Graduate Studies and Research

Prof. Dr. Ali Hakan Ulusoy
Director

I certify that this thesis satisfies all the requirements as a thesis for the degree of Doctor of Philosophy of Civil Engineering.

Assoc. Prof. Dr. Eriş Uygar
Chair, Department of Civil Engineering

We certify that we have read this thesis and that in our opinion it is fully adequate in scope and quality as a thesis for the degree of Doctor of Philosophy of Civil Engineering.

Prof. Dr. Umut Türker
Supervisor

Examining Committee

1. Prof. Dr. Mustafa Ergil
2. Prof. Dr. Serdar Korkmaz
3. Prof. Dr. Mehmet Sorgun
4. Prof. Dr. Umut Türker
5. Asst. Prof. Dr. Hasan Zaifoğlu

ABSTRACT

Debris flow is a geological hazard characterized by the irreversible deformation of sediment and water mixture. Due to its highly destructive potential, especially with the rise in the frequency of intense rainfall events and urbanization in hilly and mountainous areas, it is crucial to implement effective measures to reduce the debris flow risk. To mitigate debris flow disasters, most of the previous research has focused, mostly through experimental methods, on placing different rigid barriers as structural prevention against debris flow to dissipate its energy. On the other hand, simulating debris flow resistance on the tree trunk patches has received little attention. In the present work, analytical and numerical simulation of the peak impact pressure of debris flow on a vertical rigid wall has been analysed under the protection of a patch of tree trunks. Along the debris flow path, tree trunks with identical diameters have been arranged in linear and rectilinear configurations. The mathematical analysis employs the Reynolds Transport Theorem, while the numerical simulations use the Reynolds-Averaged-Navier-Stokes equations. Numerical simulations have shown that a rectilinear arrangement of tree trunks in a designated area is more effective than other configurations. Additionally, increasing the density of tree trunks within a specified area provides 50% more protection compared to simply adding more rows of tree trunks. Additionally, this study estimates a new dynamic coefficient (α) based on the Froude number and devises a new expression for the drag force coefficient for different tree trunk configurations.

Keywords: Debris Flow, Rigid Barriers, Tree Trunks, Reynolds Transport Theorem, Reynolds-Averaged-Navier-Stokes.

ÖZ

Enkaz akışı, çökelti ve su karışımının geri döndürülemez deformasyonu ile karakterize edilen jeolojik bir tehlikedir. Özellikle aşırı yağış olaylarının artması ve dağlık bölgelerde kentleşmenin artmasıyla birlikte, son derece yıkıcı potansiyeli nedeniyle, enkaz akışı riskini azaltmak için etkili önlemlerin uygulanması büyük önem taşımaktadır. Enkaz akışı felaketlerini azaltmak için önceki araştırmaların çoğu, deneysel yöntemlerle, enkaz akışına karşı enerjisini dağıtmak için yapısal önleme olarak farklı sert bariyerler yerleştirmeye odaklanmıştır. Ancak ağaç gövdesi kısımlarında moloz akışı direncinin akima olan etkisi konusunda daha az araştırma yapılmıştır. Bu çalışmada, dikey sert bir duvar üzerindeki moloz akışının tepe darbe basıncının analitik ve sayısal simülasyonu, bir ağaç gövdesi parçasının koruması altında analiz edilmiştir. Enkaz akış yolu boyunca aynı çaplara sahip ağaç gövdeleri doğrusal ve doğrusal konFigure ürasyonlarda düzenlenmiştir. Matematiksel analizde Reynolds Taşıma Teoremi kullanılırken sayısal simülasyonlarda Reynolds-Ortalamalı-Navier-Stokes denklemleri kullanılmıştır. Sayısal simülasyon sonuçları, belirli bir alanda ağaç gövdelerinin doğrusal konFigure ürasyonunun diğer konFigure ürasyonlara göre daha etkili olduğunu ve belirli bir alanda ağaç gövdelerinin yoğunluğunun arttırılmasının, ağaç gövdelerinin sıra sayısındaki artışa göre %50 daha fazla koruyucu olduğunu göstermiştir. Ayrıca bu çalışma, Froude sayısının bir fonksiyonu olarak yeni bir dinamik katsayı (α) önermiş ve farklı ağaç gövdesi konFigure ürasyonları için sürükleme kuvveti katsayısı için yeni bir ifade tanımlamıştır.

Anahtar Kelimeler: Enkaz Akışı, Sert Bariyerler, Ağaç Gövdeleri, Reynolds Taşıma Teoremi, Reynolds-Ortalamalı-Navier-Stokes.

AKNOWLAGMENTS

First and foremost, I would like to express my deepest gratitude to my supervisor, Prof. Dr. Umut Türker, for their invaluable guidance, support, and encouragement throughout my research journey. Their insights, expertise, and patience have been instrumental in the completion of this thesis. I am truly grateful for the opportunity to learn and grow under their mentorship.

I would also like to extend my heartfelt thanks to my family and friends, whose unwavering love, patience, and encouragement have been my foundation throughout this attempt***. In particular, I want to express my deepest appreciation to my late father, whose constant support and belief in me was a source of strength. Although he could not witness my defense, I know his spirit has been with me every step of the way, and this achievement is as much his as it is mine.***

This thesis is based on the article that was published in the Turkish Journal of Civil Engineering (Ahmadian and Turker, 2024). The research presented in that article forms the core of this work, and I am grateful to everyone who contributed to its publication.

Thank you all for making this achievement possible.

TABLE OF CONTENTS

ABSTRACT iii

ÖZ iv

AKNOWLAGMENTS vi

LIST OF TABLES ix

LIST OF FIGURES x

1 INTRODUCTION 1

1.1 Debris Flow Definition and Morphology 1

1.2 Debris Flow in General Initiation and Growth 4

1.3 Characteristics and Classification of Debris Flows 5

1.4 Debris Flow Impact Forces 6

1.5 Debris Flow Mitigation Methods 9

1.5.1 Structural (Active) Measures 10

1.5.2 Non-Structural or Passive Measures 11

1.6 Debris Flow Mitigation Methods by the Implementation of Baffle Arrays 13

1.7 Debris Flow Mitigation Methods by the Implementation of Vegetated Cover 17

2 METHODOLOGY 21

2.1 Overview 21

2.2 Momentum Conservation Law 23

2.2.1 Reynolds Transport Theorem 23

2.3 Cauchy Momentum Conservation 25

2.4 Forces Definition 28

2.5 Model Progress 30

2.5.1 Drag Force 30

2.5.2 Tree Trunk Patches Methods 31

3 MODEL SETUP 37

3.1 Overview 37

3.2 Experimental Study Description 38

3.3 Simulation Setup 40

3.3.1 Debris Flow Particle Size Distributions.. 40

3.3.2 Boundary Condition for Model Validation 42

3.3.3 Initial Conditions for Model Validation.. 42

3.3.4 Generation Mesh for Validated Model 43

3.4 Validation of Simulations with Experimental Results. 44

3.5 Numerical Model Description with Tree Trunk Patches 51

3.5.1 The Geometry and Boundary Condition of Numerical Analysis 52

3.5.2 Mesh Generation of Fluid Domain 53

4 SIMULATION AND ANALYTICAL RESULTS 57

4.1 Overview 57

4.2 Impact Pressure Without Tree Trunk Patches... 57

4.3 All Forces that Act on the Vegetated Area within the Control Volume 59

4.4 Impact Pressure on Vertical Rigid Wall by Using Tree Trunk Patches............ 62

4.5 Normalized Drag Coefficient 67

5 CONCLUSION 74

5.1 Discussion 74

5.2 Conclusion 77

REFERENCES.. 79

APPENDIX 95

LIST OF TABLES

Table 1: Debris flows physical and mobility properties (Iverson, 1997)..................... 6

Table 2: Plan view of cylinder tree trunks arrangement in simulation model 35

Table 3: volumetric consideration of particle contents 41

Table 4: Debris flow discharge timetable for simulation analyses 43

Table 5: Debris flow simulation input variable... 44

Table 6: Drag force empirical coefficient (α) as the function of the Froude number based on experimental and analytical results 50

Table 7: Number of cell counts per meter for different tree trunk configurations..... 54

Table 8: Analytical results for both group models A and B. 60

Table 9: Numerical results for both group models A and B. 65

Table 10: Results of C_D, η and C_{DN} with different solid volume fraction number of rows 70

LIST OF FIGURES

Figure 1: An example of a debris flow surge (adapted from Jakob et al., 2005 by Peterson, 1986).. 4

Figure 2: Classification of debris flow as a) Stony-type debris flow in Alpine areas, (Lorenzo Marchi, n.d.), b) Turbulent muddy debris flow type in Southern California, (Guilinger, n.d.), and c) Viscous debris flows in the Alpine areas, (Lorenzo Marchi, n.d.) 5

Figure 3: A grid dam was built along the Hirayu River in Gifu Prefecture, Japan, to prevent debris flow that could cause a sediment disaster downstream (Shrestha et al., 2008), b) Slit dam constructed at the Rerukomabetsu River, Hokkaido Prefecture Japan(Nakagawa et al., 2002), c) Closed dam constructed at Khahare Khola stream in Muglin-Narayanghat Highway, Nepal (Department of Water-Induced Disaster Prevention, Nepal) and (d) Net dam constructed in the north of Thailand,(Khonkaen & Cheng, 2011).. 11

Figure 4: Debris flow passive mitigation method a) Vegetative barriers (Passive Method, Vegetative Barriers, n.d.), b) Sediment retention ponds, (Sediment Control Practices, n.d.)... 12

Figure 5: Baffles used in Hong Kong to mitigate debris flow disaster in conjunction with a rigid barrier (Yang et al., 2021).. 15

Figure 6: baffles placed in open channel to mitigate debris flow (Sham Tseng Shan Tsuen, Hong Kong), (Yang et al., 2021)... 16

Figure 7: Debris flow captured behind trees a) which is taken from Booth et al.,(2020) and b) taken from Wilford et al., (2005) 18

Figure 8: Sketch of the flume geometry and the total forces that act on the control volume attributed to the tree trunk patches arrangement at an inclined bed with the angle of (θ). 25

Figure 9: The top view of the six different linear patches of tree trunk arrangements for model group "A (A1, A2, A3, A4, A5 and A6). 32

Figure 10: The top view of the six different linear patches of tree trunk arrangements for model group B (B1, B2, B3, B4, B5 and B6)... 33

Figure 11: Debris flow experimental model with five impact sensors or load cells at the end of flume (Cui et al., (2015)).. 39

Figure 12: Debris flow simulation model geometry with various boundary condition types and 5 measurement points (historical probes) on the rigid wall. 40

Figure 13: Debris flow cumulative grain size distribution.. 42

Figure 14: The pressure distributions in the 5 measurement points on the rigid wall for clean water model based on experimental data 45

Figure 15: The pressure distributions in the 5 measurement points on the rigid wall for debris flow model based on experimental data 45

Figure 16: Impact pressure determination for different measurement points (1.5 cm, 4.5 cm, and 7.5 cm above the flume bed) that placed at different height, (a) clean water, (b) debris flow 47

Figure 17: Validation of experimental data based on simulation analysis for different measurement points (1.5 cm, 4.5 cm, and 7.5 cm above the flume bed) that were placed at different height, for a) Clean water and b) Debris flow 48

Figure 18: Analytical and experimental relationships between empirical coefficients and Froude number 51

Figure 19: Relationship between empirical coefficients and Froude number based on Analytical and experimental results for Fr between 2.5to 5.9. 51

Figure 20: Debris flow simulation model Geometry with various boundary condition types and 18 measurement points (historical probes) on the rigid wall. 53

Figure 21: Computational mesh grid of the simulated model in the control volume with two different adding mesh block (a) and (b): section a) top view, section b) side view and section c) 3D view. 55

Figure 22: The pressure distributions in the 12 measurement points (S1 to S12) on the rigid wall for without stems models 58

Figure 23: Debris flow impact Pressures at measurement points (S1 to S112) were placed at different depths for model without stems. 58

Figure 24: Debris flow impact Pressures at all measurement points (S1 to S18) placed at different depths for model A4. 61

Figure 25: Debris flow impact Pressures at all measurement points (S1 to S18) placed at different depths for model B5. 61

Figure 26: Arranging the tree trunk patches for both models A6 and B6 63

Figure 27: The pressure distributions in the 18 measurement points on the rigid wall for group models A with various tree trunks density (1.3, 2.84, 11.1, 16 and 44.4, m^{-1}) and solid volume fractions (0.98, 1.96, 3.9, 7.8, 15.7 and 31.4, %). 66

Figure 28: The Pressure distributions in the 18 measurement points on the rigid wall for group models B with various Vegetated length parameter, ∅ (0.04, 0.12, 0.2, 0.31, 0.47 and 0.67)... 67

Figure 29:. Variation of normalized drag coefficient C_{DN} with various row numbers Nr for group model B. 71

Figure 30: Variation of normalized drag coefficient C_{DN} with various solid volume fraction ψ for group model A (Linear and Rectilinear). 71

Figure 31: Comparison between the normalized drag coefficients C_{DN} and the estimated C_{DN} based on the results which obtained from Eq.38 and Eq.39 for both group models A and B. 72

Figure 32: The correlation between the Froude number (Fr) and dynamic empirical coefficient, (α)... 73

Chapter 1

INTRODUCTION

1.1 Debris Flow Definition and Morphology

Based on the National Research Council (NRC) (Areas (1982)), the mudfloods, mudflows, and debris flows have been classified as hyper-concentrated sediment flows. Based on the dominant shear stress from these three components, Julien and Leon (2000) offered a classification of hyper-concentrated sediment flows in debris flow in which dispersive stress is dominant. High-density mixtures of water and sediment movement along the seafloor or riverbed are called hyper-concentrated sediment flows, or hyperpycnal flows. These flows occur when sediment concentrations in the water exceed the critical threshold for keeping sediment particles suspended. The hyper-concentrated sediment flows usually occur in places where there is a large amount of sediment input into the water, including river deltas, estuaries, or regions that get a lot of rain or meltwater from glaciers. These high sediment concentrations may be the cause of erosion, landslides, or sediment resuspension from the seafloor or riverbed. These flows can also cause hazards to infrastructure and human activities in mountainous and coastal areas. Therefore, it is crucial to comprehend the dynamics of hyper-concentrated sediment flows in order to manage damaged areas and reduce the risks connected to these occurrences.

A debris flow is a type of geological hazard that is intermediate between hyper-concentrated flows (intense bed load transport) and landslides. It is characterized by sharp transitions in flow type, celerity, and deposit nature in terms of mass movement (Iverson, 1997)Generally, the type of landside refer to all type of surface movement. The solid fraction and the material type are two key parameters for the practical classification of the debris flow (Coussot & Meunier, 1996)

Oldrich Hungr, (2000) indicated that debris flow occurs when non-plastic and saturated debris flow move rapidly through a steep channel. Debris flow involves the entrainment of saturated debris from its path, surging, internal sorting, and mixing with surface water. Debris flow is a channelized flow, even if may be initiated by the debris avalanche.

The definition of debris flows is relevant depending on the sizes and distributions of the constituent materials, the concentrations of sediment in the flow, the characteristics of the interstitial fluid, or the hydraulic parameters of the flow, such as depth, velocity, and gradient of the channel slope. However, depending on these variables, debris flows behave differently and have different damaging capacities (Takahashi, 2014).

According to Lo (2000) explanation, the processes of debris transport and landslides are governed by four main mechanisms. These are the following: deposition of the debris, erosion of the natural terrain and entrainment of more debris, transport of the mobilized debris, and initiation (or initial failure of the slope in the source location). Depending on the type of landslide, some of these mechanisms might not exist or just have a minor impact. The dominance of each mechanism differs in various zones of the path traversed by the debris, which can be categorized into three main zones: initiation, transportation erosion, and deposition (Lo (2000)).

Takahashi (2014) describes three primary mechanisms for generating debris flow:

a) Erosion of the bed deposit brought on by an external debris supply

b) Triggered by a landslide mass

c) The sudden burst of a debris flow dam.

A description of the process of debris flow can be found in Jakob et al., (2005). According to their studies, a debris flow avalanche is formed if the initial, fast landslide continues downslope without restriction. The area where debris flow is initiated usually has a steep slope, ranging from 20° to 45°.

A debris flow usually moves as a surge or multiple successive surges. Debris flow surge morphology is denoted in Figure 1. They are categorized by a longitudinal sorting of sediment particles, which transfers the debris flow boulders and coarser particles towards the debris flow front and followed by a finer mass of liquefied debris. Finally, the tail consists of a dilute, turbulent debris flow of sediment particles of charged water (Jakob et al., 2005).

Referencing (Costa, 1984) another key feature of debris flows is vertical inverse grading. This phenomenon can be described to the high agitation of the bottom layer, which counteracts the weight of coarser grains, keeping them near the free surface of the flow and preventing them from falling through voids (Iverson, 1997). This kinetic sieving, combined with a vertical velocity gradient (with higher longitudinal velocities observed at the free surface), results in the longitudinal sorting of sediments (Iverson, 1997). Deposition occurs on a debris fan when confinement was lost, and the slope angle was reduced. Whenever the flow loses confinement, the slurry flow collapses downward laterally, cancelling its lateral thrust to the front. The front flow slows down, forming elongated coarse material levees (Jakob et al., 2005). These deposited coarse materials create a dam (Iverson, 1997), typically characterized by sides and steep fronts.

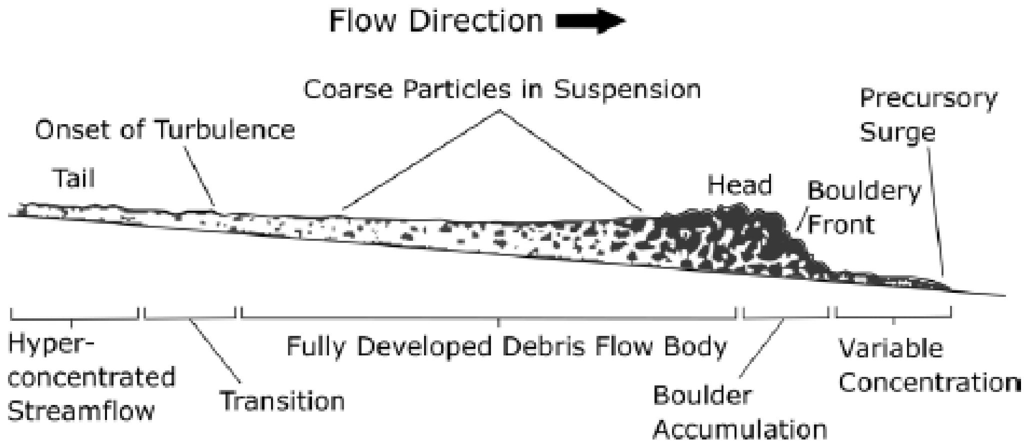

Figure 1: An example of a debris flow surge (adapted from Jakob et al., 2005 by Peterson, 1986)

1.2 Debris Flow in General Initiation and Growth

Climatic conditions and susceptibility factors influence debris flow triggering mechanisms. Two primary contributors to debris flows are extreme weather conditions, such as intense rainstorms that cause significant erosion or landslides, and soil factors, including pore pressure and saturation, which affect the likelihood of failure. Susceptibility indicates the potential volume of soil that can be entrained in the debris flow (Iverson et al., 2010 and Bel et al., 2017). Debris flows grow as a result of entrainment of material. By collapsing stream banks or by scouring the bed of the debris flow channel, this can occur. The maximum discharge of the debris flow and its runout length are mostly determined by the amount of sediment entrained, which is also a significant component in assessing the risk associated with a debris flow occurrence as it shows the affected area (Bettella et al., 2018).

1.3 Characteristics and Classification of Debris Flows

According to their appearance, debris flows can be classified as stony type, turbulent muddy type and viscous debris flow as shown in Figure 2, (Takahashi (2014)). A significant proportion of coarse materials such as gravel, rocks, and boulders within the flowing mass characterise the stony debris flow. This debris flow often occurs during heavy rainfall, snowmelt, or seismic activity, loose rocks and soil can become mobilized, forming a mixture of water, and sediment that moves rapidly in mountainous or steep terrain. Turbulent muddy debris flows contain a significant amount of fine sediment and high-water content, such as silt and clay, that are suspended within the mass of debris. However, in the viscose type of debris flow, there is a high concentration of fine-grained sediment mixed with water, which often results in dense, slow-moving masses.

Figure 2: Classification of debris flow as a) Stony-type debris flow in Alpine areas, (Lorenzo Marchi, n.d.), b) Turbulent muddy debris flow type in Southern California, (Guilinger, n.d.), and c) Viscous debris flows in the Alpine areas, (Lorenzo Marchi, n.d.)

The debris flow is commonly exemplified by a surge or a series of surges. They are characterized by a longitudinal sorting of the sediments, that transports the coarser particles and boulders to the front of flow and followed by finer debris. Finally, the tail consists of a diluted, turbulent flow of water charged with sediment (Jakob et al., 2005). According to data from Iverson (1997) the physical properties of debris flows are tabulated in Table 1.

Table 1: Debris flows physical and mobility properties (Iverson, 1997).

Property and Unit	Symbol	Typical Values
Mass Density, Kg/m^3	ρ	2500 -3000
Mean diameter, m	δ	10^{-5} - 10
Friction angle, deg	Φ_g	24 - 45
Solid volume fraction	υ_s	0.4 - 0.8
Fluid volume fraction	υ_f	0.2 - 0.6
Restitution coefficient	e	0.1 - 0.5
Magnitude, m^3	$\forall$	10^3 - 10^6
Velocity, m/s	ν	0.5 - 20
Arrival Distance, km	d	0.2 - 10

1.4 Debris Flow Impact Forces

Debris flows are a type of mass wasting event that happen when a mixture of water, soil and rock rapidly moves down a slope. These flows can cause significant damage to structures in their path, including rigid walls. In mountainous regions, buildings are the main concern when they face risks associated with debris flow disasters. In recent decades, many research studies have been done to understand, assess and eventually reduce structural exposure and vulnerability (Cui et al., 2015; Ng et al., 2017; Yang et al., 2021; Huang et al., 2022; Huang and Zhang 2022 and Yan et al., 2023).

Therefore, the determination of the debris flow impact force on any obstacle along their path should be taken as a priority (Yazid et al., 2017 and Mahnamfar et al., 2020). There are several ways to carry out and calculate the debris flow impact forces. These can be categorized as analytic formulas, experimental studies at fields or flumes, or numerical analyses based on previous studies. Previously, based on field measurements (Leonardi and Pirulli, 2020 and Yan et al., 2023) and the scaled experiments (Scheidl et al., 2012; Cui et al., 2015; Armanini et al., 2019 and Song et al., 2021) a lot of investigations about debris flow impact forces have been examined. Debris flow impact forces have been defined as the combination of slurry and grain impact loading (Lei et al., 2018). Moreover, slurry impact pressure studies can be classified into two groups: hydrostatic models and hydrodynamic models (Lichtenhahn, 1973) and Zanchetta et al., 2004).

A study by Iverson et al., (1997) observed that the pressure exerted on a wall can be several orders of magnitude higher than the weight of the flow. Similarly, another study by Xiangbo Li et al., (2011) performed a physical flume experiment and found out that the impact of debris flows on the rigid wall is greater than the weight of water.

Hong et al., (2015) determined debris flow impact pressure for 139 debris events in Jiangjia-Ravine in Yunnan Province, China, between 1961 and 2000 years. According to their field observations, the peak impact loads caused by the debris front were nearly twice as high as the remaining debris impact pressure. This is probably due to the debris flow changing velocity during various phases of impact (Hong et al., 2015).

The impact pressure of debris flow on rigid walls is affected by a variety number of factors, involving the flow velocity, particle size and composition, flow depth, and width. One of the main factors that affect the distribution of debris flow pressure on rigid walls is the change in debris flow velocity. Research by Chen et al., (2014) has shown that as the velocity of debris flow increases the pressure exerted on the wall increases. Due to the increased kinetic energy of the particles in the flow, the wall is subjected to a greater impact force.

Particle size and composition are other important factors that affect the distribution of debris flow pressure on the rigid walls. Recent related researches, demonstrated that as density and particle size of the debris flow increase, the pressure applied on a wall decreases (He et al., 2016., and Kaitna et al., 2016 and Wang et al., 2018). This occurs because larger, denser particles are less likely to be transported by the flow and tend to be deposited before they arrive at the wall. Additionally, the presence of cohesive materials like clay or silt can affect the distribution of impact pressure, with flows containing these materials experiencing less pressure than those without these materials.

Cui et al., in (2015) used a miniaturized flume experiment to carry out the measuring peak impact forces of viscous type of debris flow. In their experiment, they conducted a total of 27 tests, with a Froude number variation between 2.5 and 5.9. Subsequently, these results are compared with 155 tests of previous data with Froude number between 0.5 and 10.8. In their experimental research five impact measurement points (five sensors or load cells) S1 to S5 are located at the end of flume. These points are placed at different vertical depths from the bottom of the flume. They examined that the flow impact pressure processes can be considered into three stages. First, there is a strong impact at the head of the debris flow that was sustained for 1 second with a peak pressure impulse shape, followed by a steady impact along the body which was sustained for 3 to 4 seconds, and finally, there is a sliding flow at the tail which was sustained for 3 to 4 seconds and the velocity be much lower than other steps, and the load cells were exposed to static pressure (Cui et al., 2015).

Yan et al., in (2023) utilized real-time impact force measurements and field observations for 38 surges of debris flows which were recorded by a sensor network in Jiangjia Ravine, China, to identify the impact force distribution of natural debris flows. They observed that dense sediment concentration with high viscosity laminar flows and frequent interactions between solid particles characterize debris flows. They figured out this fluctuating force component as resulting from solid particle impacts on the sensors because it has a large magnitude and high frequency (Yan et al., 2023).

1.5 Debris Flow Mitigation Methods

Debris flow is a geological hazard characterized by irreversible sediment-water mixture deformation. It is solid-liquid two-phase flow that consists of slurry or water containing silt, clay and sand (Thouret et al., 2020). Since the kinetic energy of debris flow is very high, its interaction with engineering structures along their paths can be devastating (Armanini 1997). Extreme impact force causes serious damage that can even end in societal disasters. Therefore, debris flow has a high destructive potential and must obtain effective countermeasures to reduce the risk.

Structural (active) and non-structural (passive) measures are often required to mitigate their impact. Non-structure methods generally do not require direct engineering but can involve land use regulation education (e.g. land use planning and no build zone). Alternatively, the structure methods involve engineering work and aim to upgrade work on the slope to reduce the probability of failed or defensive measures to the consequences of potential failures (Lo (2000)). Figure 3 illustrates some examples of structure methods like different check dam types that are located in diverse geographical regions. Countermeasures designed to mitigate the debris flow disasters for structural or non-structural methods can be classified as below:

1.5.1 Structural (Active) Measures

a) Debris Basins: A debris basin or retention structure is constructed to prevent debris flows from reaching downstream areas. Sediment removal systems are typically included in these basins to maintain their effectiveness over time.

b) Debris Nets: Steel cables or synthetic fibres are used in fences or nets to prevent debris from reaching vulnerable areas.

c) Check Dams: Reducing debris flow velocity, slowing down sediment transport, and capturing debris through the construction of small dams.

d) Channelization: The construction of natural channels or the modification of natural channels to solve down the impact of debris flows on surrounding infrastructure and communities.

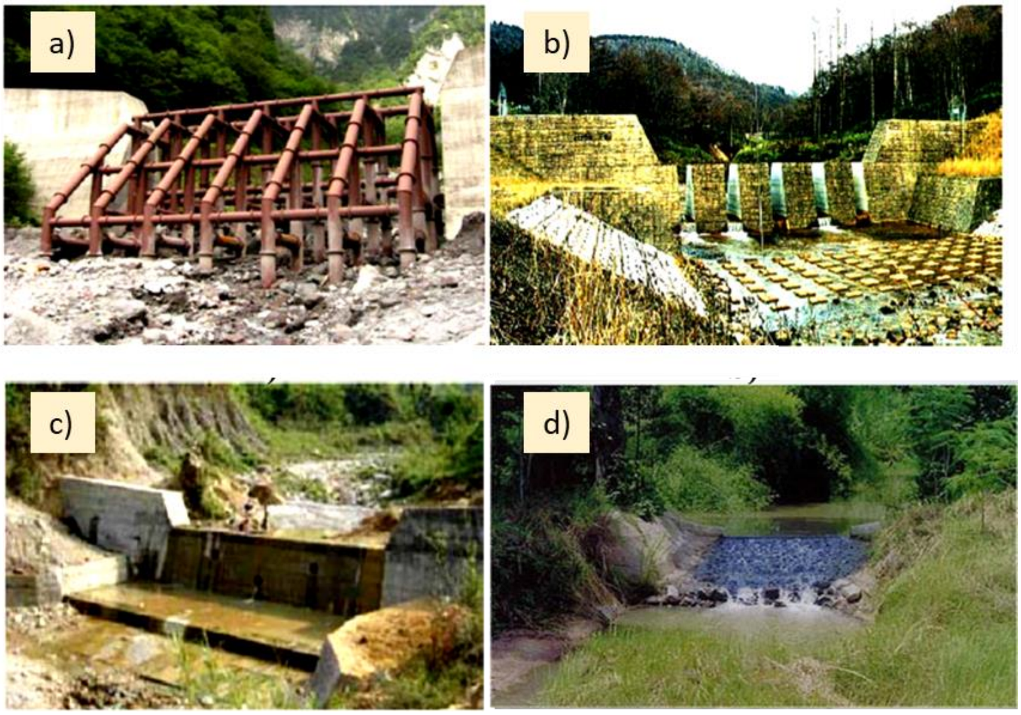

Figure 3: A grid dam was built along the Hirayu River in Gifu Prefecture, Japan, to prevent debris flow that could cause a sediment disaster downstream (Shrestha et al., 2008), b) Slit dam constructed at the Rerukomabetsu River, Hokkaido Prefecture Japan(Nakagawa et al., 2002), c) Closed dam constructed at Khahare Khola stream in Muglin-Narayanghat Highway, Nepal (Department of Water-Induced Disaster Prevention, Nepal) and (d) Net dam constructed in the north of Thailand,(Khonkaen & Cheng, 2011)

1.5.2 Non-Structural or Passive Measures

Figure . 4 presents examples of non-structural methods used to mitigate debris flow, such as various types of vegetative barriers and retention ponds. There are several non-structural measures to counter debris flow that can named as below:

a) Land Use Planning: Implementing land use and zoning regulations to restrict development in high-risk areas prone to debris flows. Maintaining buffer zones around steep slopes and watercourses is part of this process.

b) Vegetation Management: To reduce the likelihood and magnitude of debris flows, natural vegetation cover is preserved or restored in high-risk areas to stabilize slopes, reduce erosion, and enhance infiltration capacity.

c) Early Warning Systems: They are monitoring networks and early warning systems to detect debris flow precursors, such as soil moisture levels, rainfall intensity, and ground movement. At-risk communities can take protective measures and evacuate if early warning systems provide timely alerts.

d) Public Education and Awareness: Campaigns to raise awareness of debris flow risks and educate communities about evacuation procedures, emergency preparedness, and land use practices that can mitigate hazards.

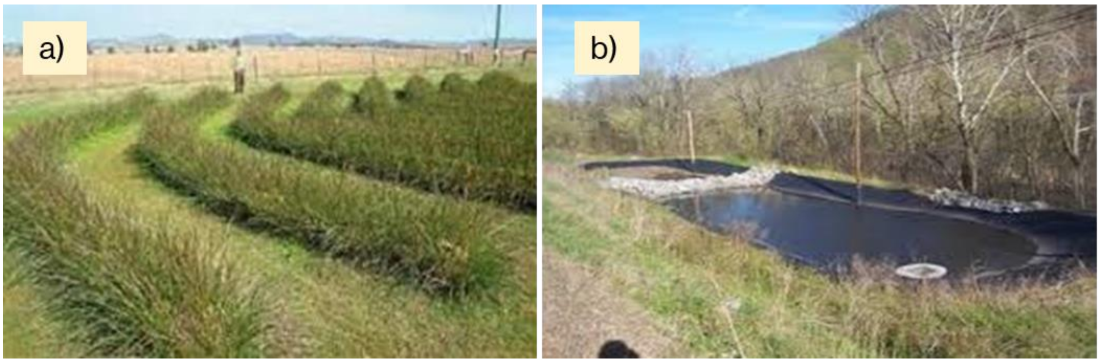

Figure 1: Debris flow passive mitigation method a) Vegetative barriers (Passive Method, Vegetative Barriers, n.d.), b) Sediment retention ponds, (Sediment Control Practices, n.d.)

Much research have been done over the years to dissipate debris flow energy using various measurement methods through experimental and theoretical analysis. Most of the previous research has focused on placing different rigid wall barriers such as grid, slit and close dams and also flexible barriers like net dams as structural prevention against debris flow to dissipate its energy (Jakob et al., 2005; Hungr et al., 2014; Takahashi, 2014; Song et al., 2021 and He et al., 2022). Referring to their research, several important factors must be measured to ensure the effectiveness of these dams. These can be the appropriate design for bearing the forces of the debris flow, the location where the dam can intercept and reduce debris flow effectively, the dimensions of the check dam such as height and size that handle the expected volume of debris flow and can be able to store flow sufficiently and trap the sediment effectively.

A study by Tang & Hu in 2018 demonstrated that debris flow impact pressure on the barriers does not only based on debris flow dynamics but also depends on the barrier material properties. Tang & Hu, 2018 utilized twenty-five tests with different kinds of barrier materials such as black granite, steel, white granite, marble and polyvinyl-chloride (PVC) board. They examined that the barrier materials with low mechanical impedance, compared to materials with high mechanical impedance, elastic stress waves travel through a structure more slowly, resulting in lower impact pressure from debris flows. Hence, using flexible materials to ensure strength while reducing the impact pressure of debris flows is more advantageous (Tang & Hu, 2018).

Generally, it is more efficient to use flexible check dams versus closed dams for mitigating debris flow energies (Xiong et al., 2023). The flexible dam can dissipate debris flow energy more effectively and minimise the structural damage. Flexible dams are also more resilient than closed dams, as they deform under the pressure of debris flow compared with closed dams. In addition, unlike closed dams, flexible dames are able to trap larger debris while allowing water and finer particles to pass through.

1.6 Debris Flow Mitigation Methods by the Implementation of Baffle Arrays

To mitigate the disasters, most of the previous researchers have focused on placing different dams as rigid barriers which are taken as structural prevention against debris flow disasters to trap the soiled materials. Also, the construction of a concrete baffle array is an alternative way to minimize the destructive effect of debris flow (Armanini et al., 2005; Remaître & Malet, 2010 and Huang & Zhang 2022).

The baffle structure contributes to reduce debris flow mobility and reduce the triggering capacity of the debris flow. The presence of the baffles increases the debris flow resistances, prevents debris flow from moving, supports the deposition of debris, and most importantly, reduces the maximum impact forces on structures. In this kind of structure, the height, type and distance between each baffle play an essential role in mitigation purposes. In general, scientists prefer to perform numerical simulation or fieldwork to determine the performance of baffle structures (Ng et al., 2015; Bi et al., 2018; Wang et al., 2020; Yang et al., 2021; Deng et al., 2022; Kim & Yune 2022 and Kim et al., 2023). Numerous studies have studied baffles constructed at slopes where granular flows are accelerated (Choi et al., 2015) and at deposition zone where granular flows are decelerated (Wang et al., 2020).

A series of physical tests were carried out by Ng et al., (2015a) to investigate the reduction in flow velocity of granular flows after passing through the baffle structure. Their findings indicated a substantial 57% reduction in frontal velocity with the implementation of three baffle arrays.

The optimal baffle array distance, height, and space have all been determind by "numerous numerical modelings and physical experiments" (Choi et al., 2015; Ng et al., 2015al and Bi et al., 2018). These studies also examined how the impact of the baffle structure affacts the run-out and also impact of the rock avalanche under the conditions of prototypical.

The effectiveness of arc-shaped baffles in controlling the deposition of rock avalanches was demonstrated by Wang et al., (2020). Also, study by X. Li et al., (2020) contributed to the rational design of baffle structures. The primary focus of these studies has revolved around optimizing baffle conFigure urations by adjusting parameters such as baffle shape column spacing, height, or array distance. Moreover, indicators including run-out distance, deposition spot, and reduction of flow velocity have been used to measure how well these optimized baffle arrangements work.

Yang et al., (2021) examined how granular flow was affected by check dams and baffle systems. They investigated how installing baffles in front of check dams or any other rigid barriers can diminish design loads and change size of the rigid barriers. Additionally, they have been found that raising the baffles height increases baffle effectiveness. The efficiency of the baffle is particularly increased by raising it to around 2.7 times the maximum depth of the approaching flow without baffle. Also, This increase prevents some of the granular flow from passing over the baffle unrestricted. Figure 2 and Figure 3 demonstrates the baffle used in Hong Kong with a rigid barrier (Yang et al., 2021).

Figure 2: Baffles used in Hong Kong to mitigate debris flow disaster in conjunction with a rigid barrier (Yang et al., 2021)

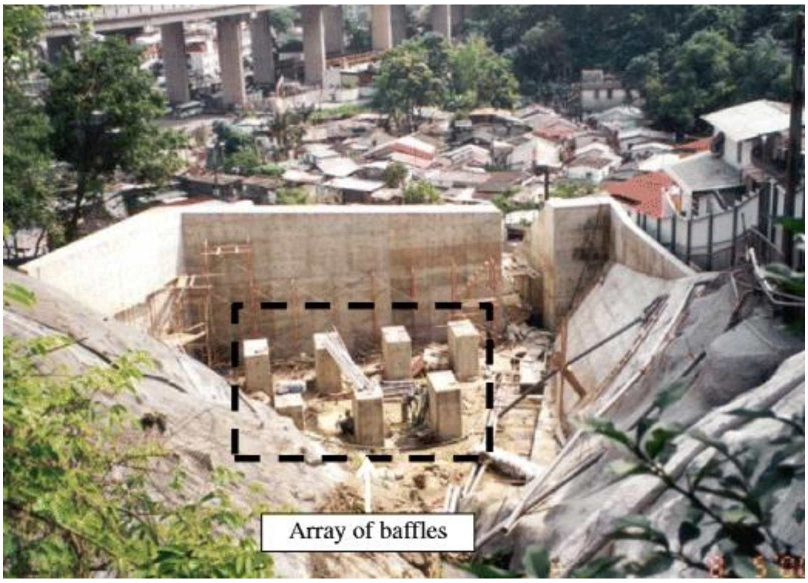

Figure 3: baffles placed in open channel to mitigate debris flow (Sham Tseng Shan Tsuen, Hong Kong), (Yang et al., 2021)

Kim et al., (2023) examined the debris flow dynamic impact load and energy dissipation on the group of cylindrical baffles by small scale flume expriments with various baffle heights and conFigure urations. Additionally, large scale expriments were analyzed to verify the results and assess the scale effect on flow characteristics. The results show that the use of taller baffles, in comparison with shorter baffles, decreased the velocity of debris flow after passing through the array of baffles by 33%. When the number of taller baffle rows is increased from 2 to 4, the velocity is lowered by 41%. For the large scale expriment velocity was further reduced by 32% when the number of baffle rows was increased from 2 to 4. Additionally, when the height of baffle increased from 40 mm to 80 mm, the energy loss increased by 35% for cases with two rows of baffles. Furthermore, An average of 21% more energy was dissipated per row of baffles when the rows number increased from 2 to 4. Like the small scale expriment, the large scale expriment performed an additional 20% energy loss by increasing the row numbers of baffles (B.-J. Kim et al., 2023).

1.7 Debris Flow Mitigation Methods by the Implementation of Vegetated Cover

Similar to baffle array structures, a patch of trees (in cases of rigid vegetation) can also contribute to reduce debris flow mobility and reducing the triggering capacity of the debris flow. The presence of the tree trunks increases the debris flow resistance, supports the deposition of debris, and most importantly, reduces the maximum impact forces on structures (Fidej et al., 2015 and Bettella et al., 2018).

In addition, interest has recently been increasing in the study of tree trunks or vegetation in debris flow disasters to dissipate debris flow energy on their paths. In recent years, the impact of trees on debris flow deposits has been extensively studied. Researchers have been studying how tree trunks (in cases of rigid vegetation) affect the flow patterns in rivers, streams, coastal dunes and floodplains (Mashud et al., 2011; Vargas-Luna et al., 2015; Türker et al., 2019 and Kumar et al., 2021), but few studies investigated the effect of a patch of trees as a preventive measurement against debris flow disaster. The rigid vegetation or tree trunks exert drag forces against debris flow that can greatly reduce debris flow velocities near the bed (Liu et al., 2021) and also can reduce suspended sediment transport and sediment erosion (Vargas-Luna et al., 2015 and Kang et al., 2022). The majority of experimental and theoretical studies of cylinder arrays (representing vegetation canopies or tree trunk solid fraction) have been addressed for water flow. These research studies have consistently shown the effect of canopy density on the drag coefficient and water flow velocity (Tanino et al., 2008; Etminan et al., 2017; D'Ippolito et al., 2019; Chang et al., 2020; M.-Y. Liu et al., 2020; Mancheño et al., 2021 and Sohrabi et al., 2023). Tree trunks increase flow resistance by exerting drag forces, as a result, the mean debris flow velocity and bed shear stress are reduced so that the water levels become high. Additionally, the tree trunk forces the flow to move around, which changes the flow field around tree trunks (Nepf, 2012 and Liu at al,. 2016).

Figure 4 depicts how deposits are left behind when the debris flow has passed and illustrates how debris is trapped behind a tree. The arrow in the lower-right corner of Figure 4a indicates the debris flow direction. As seen in Figure 4b trees and entrained logs can stop the flow and capture sediments behind the barrier from upstream of the trees. (Booth et al., 2020 and Wilford et al., 2005).

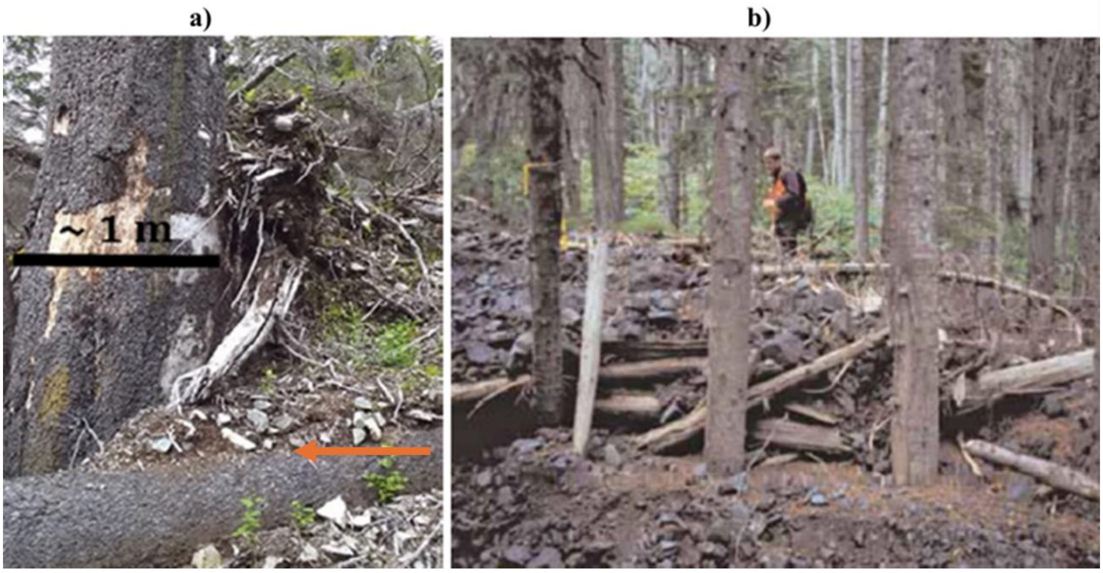

Figure 4: Debris flow captured behind trees a) which is taken from Booth et al.,(2020) and b) taken from Wilford et al., (2005)

Research studies by Etminan et al., (2017) and Liu et al., (2020), indicated that the flow behaviour in rivers, streams and floodplains are significantly influenced by vegetation canopies, principally due to the cumulative drag forces. They found that blockage effect with high vegetation densities had a greater impact on reducing drag coefficient than sheltering effects in staggered configurations. However, in the linear configuration with a constant blockage ratio, the sheltering effect was stronger. The sheltering effect refers to the protection or reduction in fluid force experienced by the downstream vegetation canopies due to the upstream vegetation interference with the flow. It means that one body is located in the wake region of the upstream body, where the downstream body experiences a lower incident velocity than the upstream body. The blockage effect refers to the lateral distance that each vegetation canopies have on the flow field due to their presence, which causes the fluid to be diverted around them.

In New models for predicting canopy drag coefficients are proposed based on the mechanisms that explain the canopy of flow resistance (Etminan et al., 2017 and Liu et al., 2020).

Sohrabi et al., (2023) examined the drag coefficient as a parameter to denote the flow resistance in emergent and submerged of vegetation patches with various densities by using the method of balance approach-blockage factor. They have investigated the four vegetation emergent patches with varieties densities, configuration, random, tandem and circular. Their finding denoted that the drag coefficients of vegetated patches with random type were larger than those vegetated patches with tandem type. Also, there was a direct relationship between the drag coefficient and vegetation density. All patches had the highest flow resistance in the initial rows, so the drag coefficient decreased through vegetation patches (Sohrabi et al., 2023).

There is still an incomplete understanding of the morphologies of debris flow behaviour, and fewer studies have addressed patches of tree structures and their interactions within debris flow material along with their travel distances. The experimental analyses by considering the assumptions about the material concentration, particle size distribution and rheological parameters alone can be inaccurate in measuring the impact force of debris flows. A variety of factors might cause to inaccuracies, including environmental conditions, human error during experiments, variations in the frequency of debris flows, and discrepancies in devices and testing methods. Therefore, making accurate numerical analysis and an analytic method can be effective ways to obtain accurate debris flow impact force.

In the present work, an analytical investigation and a numerical evaluation are conducted to compare the behaviour of debris flow, its impact force and distribution when it encounters a rigid wall by comparing results from several previous large-scale and small-scale laboratory experiments. The theoretical analysis is evaluated by the Reynolds Transport Theorem (RTT) that passes through the selected control volume by representing the amount of conservation of mass, momentum and energy. The simulation results are analysed by FLOW-3D, a three-dimensional finite element model which gives value to insight into several physical flow processes. The Renormalized Group (RNG) k-ε model is used as a turbulence model. This model is the most precise, highly suitable and robust model for accurately simulating mass flow dynamics. To offer better coverage, it expands the capabilities of the standard k-ε model. Basically, the Navier-Stokes equations which describe the motion of fluids in three-dimensional space are solved and this gives the ability to measure the peak impact pressures on the rigid wall. The purpose of this study is to determine the maximum impact pressure of debris flow over a rigid vertical wall, right after passing through different configurations of patches of tree trunks. For the development of effective measures, two different configurations are simulated. In one of the simulations the number of rows of tree trunks increased towards upstream, whereas, in the second configurations, the density of tree trunks increased within a predefined area.

Chapter 2

METHODOLOGY

2.1 Overview

For calculating the peak impact pressure caused by debris flow against rigid wall barriers, the hydrodynamic (Armanini (1997)) and hydrostatic (Lichtenhahn (1973)) approaches are commonly applied in recent studies. This study presents the numerical and mathematical processes related to the maximum impact force over the rigid wall where the variation of a debris flow can be ignored in transversal direction due to dominant velocity in the vertical and horizontal directions. Also, simulates the distribution of debris flow pressure over the rigid wall by considering all characteristics of debris flows.

It assumes that the incoming debris flow arriving from upstream and impinging on a wall is a steady and homogenous flow. Hence, due to violation of backwater effects, the incoming debris flow must be supercritical flow (Iverson et al., 2016). Debris flow can be a function of significant analytic formula, Froude number (Fr), which extensively going on for characterizing kinetic energy similarity in open channel granular flows (Armanini, 1997; Scotten and Trivellato, 1995 and Tiberghien et al., 2007). The Froude number, is quantified as the ratio between the inertial and gravitational forces and is given as follows:

$$F_r^2 = \frac{u^2}{g\ H\cos\theta} = \frac{\rho u^2}{\rho g H\ \cos\theta} = \frac{\text{Inertial force}}{\text{Gravitational force}} \tag{1}$$

where u is debris flow velocity (m/s), g is the gravitational acceleration 9.81 (m/s^2), H is the vertical flow depth (m), θ is the flume bed inclination and H cosθ is named as h which is depicted in Figure 5.

Depending on the Froude number (greater or less than one) the magnitude and the behaviour of debris flow changes. In this research, the numerical analysis is based on the experimental study performed by Cui et al., (2015) where the debris flow examined under supercritical flow conditions. Hence the Froude number is always greater than 1. The debris flow generally generates high kinetic energy named as the hydrodynamic impact force. This was initially studied by Hungr et al., (1984) and later by Armanini (1997) showing that the hydrodynamic impact force is proportional to the density of debris flow and the velocity. Hence the debris flow maximum impact pressure equation is given as follows:

$$P_{dmax} = \alpha\rho\ u^2 \tag{2}$$

In which ρ is debris flow density, and α is the empirical proportionality coefficient for hydrodynamic models that can be experimentally identified according to type of debris flow. For instance, α =2.0 was suggested by Watanabe (1981) for laminar or fine aggregate debris flows, 2.0 and 4.0 were measured by (Egli, 2005) for debris flows which mainly involve coarse aggregate. Values between 3 and 5 were found from field investigations of 70 debris flow tests in China (Zhang, 1993).

Hübl et al., (2009) used dimensional analysis and proposed a method for obtaining debris flow P_{dmax} against protecting structure expressed as:

$$\frac{P_{dmax}}{\rho u^2} = a\ F_r^b \tag{3}$$

Where the parameters of (a) and (b) are empirical factors and their values are between 4.9 to 5.62 and -1.66 to -1.29, respectively (Hübl et al., 2009).

2.2 Momentum Conservation Law

2.2.1 Reynolds Transport Theorem

This study presents the mathematical processes related to the maximum impact force over the rigid wall. Referring to the definitions given by Takahashi (1979) ; Chu et al., (1995) and Mangeney et al., (2010), when the momentum of the debris flow changes, it initiates the impact impulse pressure on a rigid wall. For a general referring to Reynolds Transport Theorem from the definition of a derivative, the rate of change of $N_{sytree\ trunk}$ for non-steady-state flow in an open system is given as follows:

$$\left.\frac{\partial N}{\partial t}\right)_{system} = \frac{\partial}{\partial t}\int_{c\forall} \eta\rho d\forall + \int_{cs} \eta\rho\vec{u}\overrightarrow{dA} \tag{4}$$

In which N is extensive property and represents the amount of mass, or momentum, or energy of the control volume, η is the intensive property per unit mass which is 1, v and e for mass, momentum and energy respectively, ρ is debris flow density, the first term of equation represents the change rate of the amount of property N in the control volume, $\rho\frac{\partial m_{cv}}{\partial t}$, and the last term indicates the net rate at which property N is exiting the surface of the control volume. and $\vec{u}.\overrightarrow{dA}$ is the scalar product of velocity vector and area vector.

First, referring to the mass balance equation (MBE), the net mass transported to the control volume is equal to the net change in mass exiting the control volume at the base of the slope.

$$M)_{system} = \int_{M\ (sytree\ trunk)} 1dm = \int_{\forall\ (sytree\ trunk)} 1\rho d\forall \tag{5}$$

With this substitution, we determine:

$$0 = \rho \frac{\partial m_{cv}}{\partial t} + \int_{cs} 1\rho\vec{u}\overrightarrow{dA} \tag{6}$$

In this case, $\frac{\partial m_{cv}}{\partial t}$ is the mass differential amount for the non-steady flow. For a steady flow, there is no mass differential, therefore, the second term must equal zero and Figure ures the mass rate transfer leaving across control surface area which can be written as follows:

$$\int_{cs} 1\rho\vec{u}\overrightarrow{dA} = 0 \tag{7}$$

Based on Reynolds Transport Theorem Eq. 4 and conversation of momentum, the linear momentum of the control volume is expressed by Eq. 8 then by inserting to Eq. 4 the system rate change of linear momentum is rewritten by Eq. 9. In which $\left.\frac{\partial P}{\partial t}\right)_{system}$ is equal to the sum total of all external forces acting on the control volume which are determined by considering the equation of motion of an infinitesimal volume of fluid which expresses the Newtonian second law of motion and deals with the mechanical behavior of materials. Eq. 10 shows newton's second law of motion to fluid element which expresses the time rate of change of momentum in the control volume equivalent to the net flow of momentum through the control volume.

$$P)_{system} = \int_{M\ (system)} \vec{u}.\,dm = \int_{\forall\ (system)} \vec{u}.\,\rho d\forall \tag{8}$$

$$\left.\frac{\partial P}{\partial t}\right)_{system} = \sum F_{Net\ forces} = \frac{\partial}{\partial t}\int_{c\forall} \rho\vec{u}d\forall + \int_{cs} \rho\vec{u}\left(\vec{u}.\overrightarrow{dA}\right) \tag{9}$$

$$\left(\begin{array}{c}\text{Sum of}\\ \text{forces}\\ \text{acting}\\ \text{On CV}\end{array}\right) = \left(\begin{array}{c}\text{Time rate of}\\ \text{change of}\\ \text{momentum}\\ \text{in CV}\end{array}\right) - \left(\begin{array}{c}\text{The rate of}\\ \text{momentum}\\ \text{inflow}\\ \text{to CV}\end{array}\right) + \left(\begin{array}{c}\text{The rate of}\\ \text{momentum}\\ \text{outflow}\\ \text{from CV}\end{array}\right) \tag{10}$$

2.3 Cauchy Momentum Conservation

Due to the definition of Eq. 10 and rewriting Eq.6, the Cauchy momentum conservation equation is obtained which represents the Newtonian second low of motion as below (Malvern, 1969).

$$\rho \frac{\partial \mathrm{v}}{\partial \mathrm{t}} \mathrm{dxdydz} = \dot{\mathrm{M}}_{\mathrm{in}} - \dot{\mathrm{M}}_{\mathrm{out}} + \sum \mathrm{F_x} \tag{11}$$

In which the rate of momentum inflow to control volume ($\dot{\mathrm{M}}_{\mathrm{in}}$) in x direction is negative direction of $\rho \mathrm{v}(\mathrm{u}) \cos\theta \, \mathrm{dydz}$ and the rate of the momentum outflow from control volume is of $\left(\rho \mathrm{u}(\mathrm{u}) \cos\theta \, \mathrm{dydz} + \frac{\partial(\rho \mathrm{u}(\mathrm{u}))}{\partial \mathrm{x}} \cos\theta \, \mathrm{dxdydz}\right)$ and $\sum \mathrm{F_x}$ represents the sum of x direction forces acting on the control volume, Figure 5.

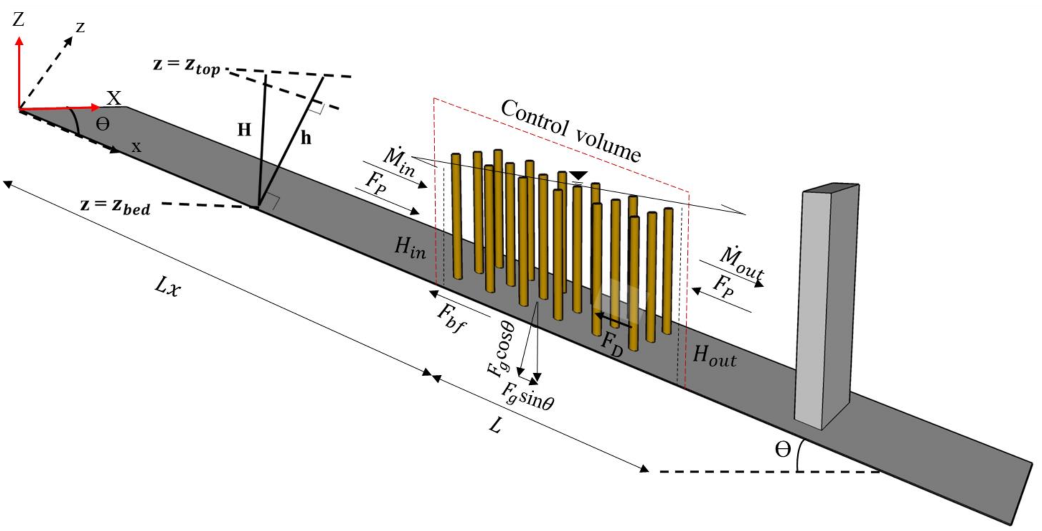

Figure 5: Sketch of the flume geometry and the total forces that act on the control volume attributed to the tree trunk patches arrangement at an inclined bed with the angle of (θ)

According to (Iverson et al., 2015) the total forces that acting on the control volume in the sloping bed at an angel θ in the x direction can be written as:

$$\sum \mathrm{F_x} = \rho \mathrm{g_x} \sin\theta \; \mathrm{dxdydz} + \left(\frac{\mathrm{d}\sigma_{\mathrm{xx}}}{\mathrm{dx}} + \frac{\mathrm{d}\tau_{\mathrm{yx}}}{\mathrm{dy}} + \frac{\mathrm{d}\tau_{\mathrm{zx}}}{\mathrm{dz}}\right) \mathrm{dxdydz} \tag{12}$$

First term is gravitational forces which represents a body force due to gravity that acts on the control volume and the second term represents external force components σ_{xx}, τ_{yx} and τ_{zy} through the control volume.

The momentum conservation is obtained by inserting Eq. 12 into Eq. 11.

$$\rho \frac{\partial \mathrm{v}}{\partial \mathrm{t}} \mathrm{dxdydz} \cos\theta$$

$$= \frac{\partial(\rho \mathrm{u}(\mathrm{u}))}{\partial \mathrm{x}} \cos\theta \, \mathrm{dxdydz} + \rho \mathrm{g_x} \sin\theta \; \cos\theta \, \mathrm{dxdydz} \tag{13}$$

$$+ \left(\frac{\mathrm{d}\sigma_{\mathrm{xx}}}{\mathrm{dx}} + \frac{\mathrm{d}\tau_{\mathrm{yx}}}{\mathrm{dy}} + \frac{\mathrm{d}\tau_{\mathrm{zx}}}{\mathrm{dz}}\right) \cos\theta \, \mathrm{dxdydz}$$

By taking depth integration of the total force equations which is bounded by moving surface at z_{top} and z_{bed} under the condition that $\bar{h} = z_{top} - z_{bed}$ and $z_{bed} = 0$, the result can be expressed by:

$$\sum \mathrm{F}_{Tx} = \rho \int_{z_{bed}}^{z_{top}} \sum F_x \tag{14}$$

After taking the depth integration from both sides of the equation, the first term can be rewritten as $\rho \frac{\mathrm{d}}{\mathrm{dt}}(\mathrm{uh})$ and the forcing term $\int_{z_{bed}}^{z_{top}} \sum F_{Tx}$ at Eq. 12 by using Leibniz rule to evaluate depth integrals can be expressed as:

$$\rho \int_{z_{bed}}^{z_{top}} \sum F_{Tx}$$

$$= \bar{\rho} g_x \sin\theta - \frac{d(\bar{\sigma}_{xx} h)}{dx} + \sigma_{xxtop} \frac{dz_{top}}{dx} - \sigma_{xx} \frac{dz_{bed}}{dx} + \frac{d(\bar{\tau}_{yx} h)}{dy} - \tau_{yxtop} \frac{dz_{top}}{dy} + \tau_{yxbed} \frac{dz_{bed}}{dy} + \tau_{zxtop} - \tau_{zxbed} \quad (15)$$

Where the $\tau_{xx} = \sigma_{xx}$ and defined as a normal stress component (Malvern 1969 and Iverson et al., 2016) and $\bar{\rho}$ is depth-averaged debris flow density which calculated by Takahashi (1979):

$$\bar{\rho} = \frac{1}{\bar{\bar{h}}} \int_{zbed}^{ztop} [\rho_w (1 - c) + \rho_m c] dz \quad (16)$$

Where $\bar{\bar{Z}}$ is mean debris flow depth thickness that bounded by z_{bed} and z_{top} ($\bar{h} = z_{top} - z_{bed}$), ρ_m is solid particles mean density, ρ_w is pure water mean density and c is dimensionless fluid volume concentration that can be calculated by Eq. 17. In which φ is the friction angle of the material that obtained from the experimental study, as shown below (Takahashi (2014).

$$c = \frac{\rho_w \tan\theta}{(\rho_m - \rho_w)(\tan\varphi - \tan\theta)} \quad (17)$$

Under the assumptions that steady flow regime is existing, the first term of Eq.11 is zero ($\frac{Dv}{Dt} = 0$), the effect of stress variation in cross slope direction can be neglected $\frac{d(\tau_{yx} h)}{dy} = 0$ and the z in the bed iz zero $z_{bed} = 0$. In this case, Eq.13 and Eq.15 can be simplified as:

$$\dot{M}_{out} = \dot{M}_{in} + \sum F_{Tx} \quad (18)$$

$$F_{Tx} = \bar{\rho} g_x \sin\theta - \frac{d(\bar{\sigma}_{xx} h)}{dx} - \tau_{zxbed} \quad (19)$$

here the F_{Tx} represents the debris flow dynamic impact against the vertical wall which is obtained by applying the conservation of mass and momentum in x-direction per unit area.

2.4 Forces Definition

Referring to Bagnold (1954) for viscosity regime in which normal stress and shear are linear functions and proportional to the shear rate du /dz, proposed relation in which the τ_{zxbed} is named basal coulomb friction force and calculated by $\tau_{zxbed} = \sigma_{zx} \tan \varphi$ (Bagnold (1954)), where φ is symbolized as a friction angle of material that it is depending on collision condition. Basal Coulomb friction refers to the resistance to motion that occurs at the base of a material in motion, typically in the context of granular flow, landslide, or debris flow. It is governed by Coulomb's law of friction, which states that the frictional force is proportional to the normal force exerted by the material on the underlying surface.

Due to the assumption that there is no acceleration happens to the bed and considering physical assumption which geostatic normal stress acting on a plane in one-dimensional stress state is σ_{zz} and given by:

$$\sigma_{zz} = \rho g_x H \cos \theta \quad (20)$$

By assuming that slope is parallel to normal stress, σ_{xx} is proportional to σ_{zz} as applied:

$$\sigma_{xx} = k\sigma_{zz} = k\rho g_x H \cos \theta \quad (21)$$

where k is the empirical proportionality coefficient. Depth integration is used for obtaining the average longitudinal normal stress $\bar{\sigma}_{xx}$ as:

$$\bar{\sigma}_{xx} = \frac{1}{h}\int_{zbed}^{ztop} k\rho g_x H \cos \theta \, dz = k\bar{\rho} g_x \bar{h} \quad (22)$$

Therefore, the Eq.12 can be reformulated by considering that F_{Tx} is the total sum of forces per unit width that acting on the control volume can be rewrite as:

$$F_{Tx} = \int_{Lx}^{L+Lx} \left[\bar{\rho} g_x \, \bar{h} \sin\theta \; - k\bar{\rho} g_x \, \bar{h} \frac{d(h)}{dx} - \bar{\rho} g_x \; \bar{h} \tan\varphi\right] dx \tag{23}$$

By considering all assumptions and substituting Eq. 23 into Eq. 18:

$$\bar{\rho} U_{in}^2 \, h_{in} + \bar{\rho} g_x \, \bar{h} \, L \sin\theta \; - k\bar{\rho} g_x \, \bar{h} L \frac{d(h)}{dx} - \bar{\rho} g_x \, \bar{h} \, L \tan\varphi = \bar{\rho} u_{out}^2 \, h_{out} \tag{24}$$

Where $\bar{\rho} U_{in}^2 \, h_{in}$, ($\dot{M}_{in}$), and $\bar{\rho} u_{out}^2 \, h_{out}$, ($\dot{M}_{out}$), are debris incoming and outgoing momentum flux per unit width, respectively, $\bar{\rho} g_x \, \bar{h} \, L sin\,\theta$, ($F_g$), is the gravitational force component per unit width, $k\bar{\rho} g_x \, hL \frac{d(h)}{dx}$, ($F_p$), is the is the longitudinal pressure force per unit width due to longitudinal variations in depth h, and $\bar{\rho} g_x \, \bar{h} \, \mathrm{L} \tan\varphi$, ($F_{bs}$), is the basal friction force per unit width.

Based on the definitions given by Takahashi (1979); Chu et al., (1995) and Mangeney et al., (2010), change on the momentum of the debris flow initiates the impact impulse pressure on a rigid wall. The total forces per unit width that acting on the control volume on the sloping bed in the x direction is:

$$F_{Tx} = \int_{Lx}^{L+Lx} \left[\bar{\rho} g_x \, \bar{h} \, sin\,\theta \; - k\bar{\rho} g_x \, \bar{h} \frac{d(h)}{dx} - \bar{\rho} g_x \; \bar{h} \tan\varphi\right] dx \tag{25}$$

Where φ represents the friction angle of the material, $\bar{\rho}$ represents depth-averaged debris flow density, $\bar{h}$ represents the depth average along the x-direction that can be written as $\bar{h} = z_{top} - z_{bed}$, L represents the control volume length and Lx is the length of the flume upstream to the control volume. The angle of inclination of bed slope is represented by θ. The first term is gravitational force which represents body force due to gravity that acts on the control volume, the second and third terms represent external force components σ_{xx} and τ_{zy} through the control volume Figure 5.

Solving Reynolds Transport Theorem to obtain the momentum flux model that is appropriate to define incoming momentum flux which flushes to downslope is given as:

$$\bar{\rho}u_{in}^2\, h_{in} + \bar{\rho}g_x\, \bar{h}L\, sin\,\theta\ - k\bar{\rho}g_x\, \bar{\mathrm{h}}L\,\frac{d(h)}{dx} - \bar{\rho}g_x\, \bar{\mathrm{h}}L\,\tan\varphi = \ \bar{\rho}u_{out}^2\, h_{o\imath} \quad (26)$$

Where $\bar{\rho}u_{in}^2\, h_{in}$, ($\dot{M}_{\mathrm{in}}$), and $\bar{\rho}u_{out}^2\, h_{out}$, ($\dot{M}_{\mathrm{out}}$), are debris incoming and outgoing momentum flux per unit width, respectively, which $h_{in} = H_{in}cos\theta$ and $h_{out} = H_{out}cos\theta$, $\bar{\rho}g_x\,\bar{h}L\, sin\,\theta$, is the gravitational force (F_g) component per unit width, $k\bar{\rho}g_x\, hL\,\frac{\mathrm{d(h)}}{\mathrm{dx}}$, is the longitudinal pressure force (F_p) per unit width due to longitudinal variations in depth h, and $\bar{\rho}g_x\,\bar{h}\,\mathrm{L}\tan\varphi$, is the basal friction force (F_{bs}) per unit width as illustrated in Figure 5.

2.5 Model Progress

2.5.1 Drag Force

Nowadays, referring to the more specific reference of the rigid vegetation field, rigid tree trunks have often been demonstrated by circular cylinders made of various materials either in experimental or simulation models. Due to the influence of the tree trunks against debris flow, the drag forces are exerted and can be expressed as $\sum_{i=1}^{N} F_D$ where N is the number of the tree trunks per unit plan area. Formally, the depth integration of drag force for a single vertical cylinder with circular shape and diameter, d, from z_{top} and z_{bed} can be expressed as:

$$F_D = \int_{zbed}^{ztop} \frac{1}{2} C_D\, \bar{\rho}u^2 d\cos\theta\, dz \quad (27)$$

In which C_D is the drag coefficient and d being the tree trunk diameter.

By inserting Eq.27 into Eq.26, the momentum conservation equation applied along flow direction given in Figure 5 can be rewritten as:

$$\bar{\rho}U_{in}^2 h_{in} + \bar{\rho}g_x \bar{h} L sin\,\theta - k\bar{\rho}g_x \bar{h}L\frac{d(h)}{dx} - \bar{\rho}g_x \bar{h}L\tan\varphi - \frac{1}{2}NC_D\, d\bar{\rho}\bar{h}u^2 = \bar{\rho}u_{out}^2 h_{out} \quad (28)$$

2.5.2 Tree Trunk Patches Methods

Several research studies have been conducted on the interaction between flow and rigid vegetation in the past (Liu et al., 2016 and D'Ippolito et al., 2021), but a few studies have been done on the effect of drag exerted from various vegetation densities on debris flow (Liu et al., 2021). Here, the tree trunk simulation analyses are based on two different scenarios. In one of the simulations, the density of tree trunks (λ) increased within a predefined area (Figure 6), and in the second configurations, the vegetated length parameters (∅) (the number of rows of tree trunks) increased towards upstream (Figure 7).

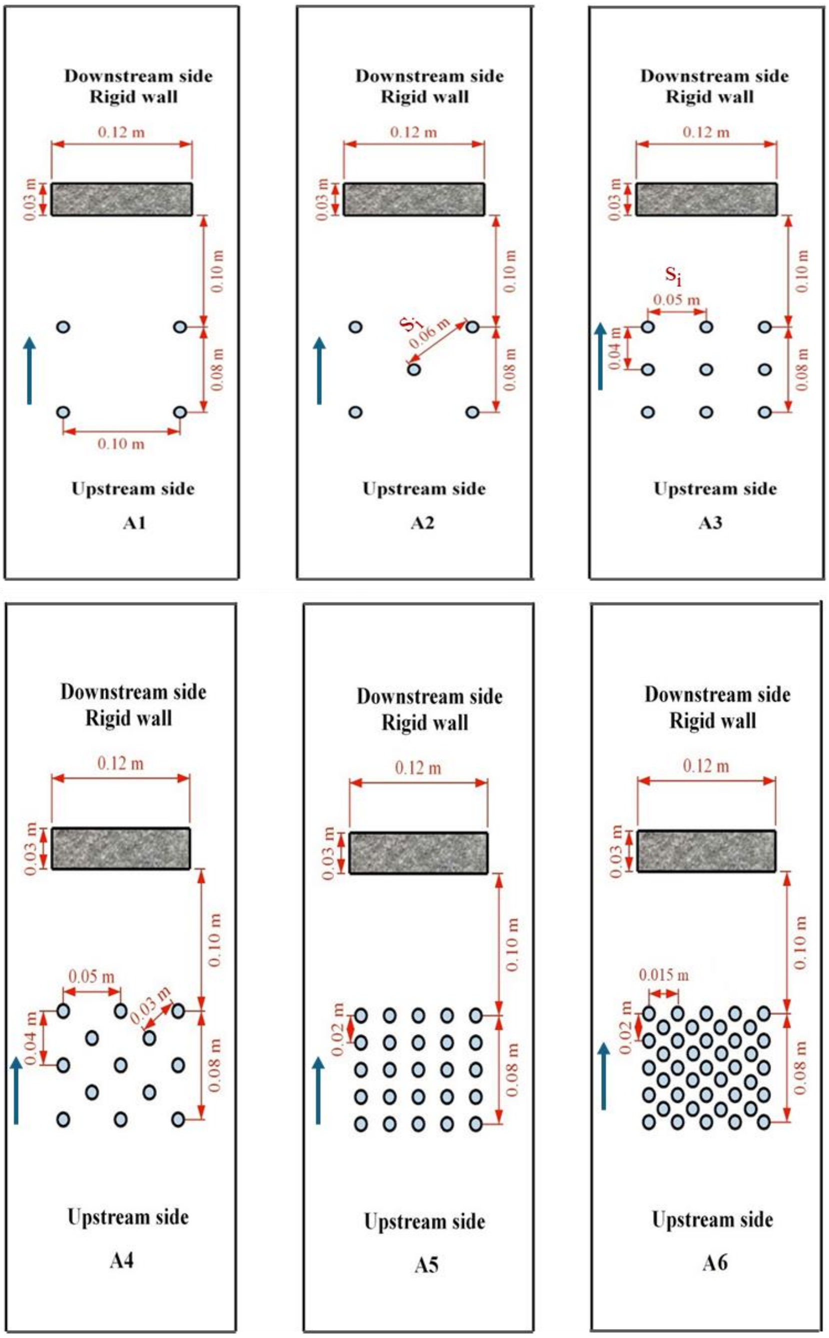

Figure 6: The top view of the six different linear patches of tree trunk arrangements for model group "A (A1, A2, A3, A4, A5 and A6).

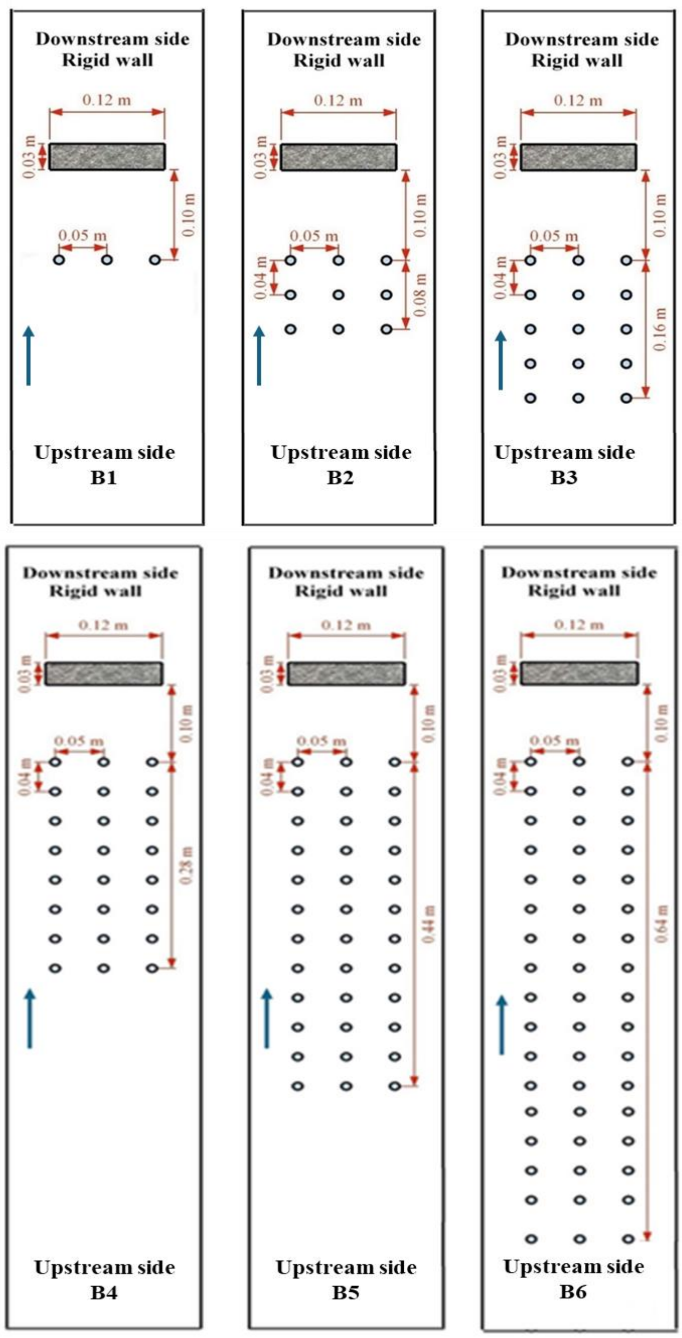

Figure 7: The top view of the six different linear patches of tree trunk arrangements for model group B (B1, B2, B3, B4, B5 and B6)

A geometric similarity ratio value of 1:50 is defined between the tree trunk diameter and the simulation model diameter. The cylinder with a 1 cm diameter and 14 cm height is simulated on the flume. The cylindrical diameter and height are sourced from Cost (1979). Tree trunk density without canopy is presented by gradually increasing the number of individual rigid tree trunk elements in the measuring plane area, in two different linear and rectilinear arrays (A1, A2, A3, A4, A5 and A6), Figure 6. In this group model two significant parameters, vegetation density (λ) and solid volume fraction (ψ), have been examined. Referring to emergent rigid vegetation for cylindrical elements with a constant diameter (d) of past experimental studies (Valyrakis et al., 2021; Wilson et al., 2003 and Nepf, 1999), by concentrating on the concept of vegetation density (λ) and based on the frontal area of the individual rigid elements per unit volume, the λ can be obtained as the ratio of the projected rigid tree trunks plan area to the total volume:

$$\lambda = \frac{dh}{s_i^2 h} = \frac{d}{s_i^2} \tag{29}$$

Where s_i represents the distance between adjacent individual tree trunk elements. The solid volume fraction is the ratio of the areal coverage of the tree trunk elements to the portion of measuring area covered by tree trunk elements previously defined by Türker et al., (2006), and expressed as:

$$\psi = N \frac{\pi d^2}{4 \Delta X \, \Delta Z} \tag{30}$$

Where ΔX is the horizontal distance, ΔZ is the vertical distance on measuring plane area and N is the number of tree trunks in the measuring area. The ΔX and ΔZ are assigned as 10 cm and 8 cm is for both group model A, respectively. Two scenarios are proposed for determining the maximum pressure applied by debris flow on vertical walls. The first scenario covers six different configurations in which linear and rectilinear patches of tree trunks are examined the tree trunk densities and solid volume fractions are ranging from λ = 1.3 m^{-1}, for the linear arrangement model A1, to λ = 44.4 m^{-1}, for the rectilinear arrangement defined as configurations A6, (Table 2).

Table 2: Plan view of cylinder tree trunks arrangement in simulation model

Model group A						
`	Tree trunk arrangement	Horizontal distance on measuring plane ΔX (cm)	Vertical distance on measuring plane ΔZ (cm)	Tree trunk distance s_i (cm)	Solid volume fraction (ψ) %	Tree trunks density λ (m^{-1})
A1	Linear	10	8	10	1	1.3
A2	Rectilinear	10	8	6	1.96	2.8
A3	Linear	10	8	5	3.9	4
A4	Rectilinear	10	8	3	7.8	11.1
A5	Linear	10	8	2.5	15.7	16
A6	Rectilinear	10	8	1.5	31.4	44.4
Model group B						
		Tree trunks spacing perpendicular to debris flow direction ΔX (cm)	Tree trunks spacing parallel to debris flow direction ΔZ (cm)	Tree trunks diameter d (cm)	Number of rows N_r	Vegetated length parameter $\emptyset$
B1	Linear	4	5	1	1	0.04
B2	Linear	4	5	1	3	0.12
B3	Linear	4	5	1	5	0.2
B4	Linear	4	5	1	8	0.31
B5	Linear	4	5	1	12	0.47
B6	Linear	4	5	1	17	0.67

The second scenario has been examined with six different configurations in which the number of rows used for the tree trunks increased towards the upstream side of the flume. The first configuration is run with one row of tree trunks (B1) and then the number of rows increased to 3, 5, 8, 12 and 17 in the following configurations, Figure 7. Spacing between each tree trunk is adjusted to ΔX =4 cm in the cross-flume and ΔZ

=5 cm along-flume directions. The dimensionless vegetated length parameter (Türker et al., 2019) ∅ is obtained by the ratio of the volume of a single vegetation element in a unit area, to the total volume of the unit area. The dimensionless vegetated length parameter varied between 0.04 and 0.67 as shown in Table 2. The vegetated length parameter, based on its definition, is calculated as given in Eq 31.

$$\emptyset = N_r \frac{\frac{\pi}{4} d^2 h}{\Delta x \, \Delta z \, h} = N_r \frac{\pi d^2}{4 \, \Delta x \, \Delta z} \tag{31}$$

Where Nr is the row number of tree trunks and h represents the height of the tree trunk.

This chapter provided a step-by-step mathematical analysis to determine the outgoing momentum flux from control volume and the relationship between all the forces that were acting on the vegetated area within the control volume. In addition, 12 various tree trunk configurations models such as linear and rectilinear for both group model A and B were introduced with different solid volume fractions and vegetated length parameters. In the linear and rectilinear configurations, the number of individual rigid tree trunk elements increased in the predefined measuring plane area, whereas in the second configurations the number of rows of tree trunks increased upstream. All simulated setups for the models using Flow 3D software are introduced and model validation is performed as is given in the following chapter.

Chapter 3

MODEL SETUP

3.1 Overview

This work aims to determine the maximum impact pressure of debris flow over a rigid vertical wall, after passing through different configurations of patches of tree trunks. The simulation results are performed by FLOW-3D, a three-dimensional finite element model which gives value to insight into several physical flow processes. In the finite element method, the physical complex structure or domain is breaks down into smaller, simpler parts called finite elements. These elements are connected at points called nodes. The prosses of breaking down the domain into elements is known as mesh generation. It then applies differential equations to each element individually.

The FLOW-3D software simulates fluid flow utilizing computational fluid dynamics (CFD). It is widely used for simulating fluid flow and related physical processes in a variety of engineering applications. FLOW-3D is particularly well suited for simulating free surface flows, where the interface between fluids (like water and air) is important, but it also analyzes complex fluid dynamics problems and handles a broad range of other fluid dynamics problems. In addition, FLOW-3D applies an easy-to-use flow interface and solvers with accurate numerical methods. The Navier-Stokes Equations are solved by FLOW-3D using a Fractional Area Volume Obstacle Representation (FAVOR) approach, defining rectangular grids as geometric regions. Continuity and momentum equations together with finite volume method are used to solve the Reynolds-Averaged-Navier-Stokes equations (RANS). The RANS equations are a set of equations used in fluid dynamics to describe the motion of fluid. These equations provide a practical way to simulate and analyze turbulent flows by averaging the Navier-Stokes equations and introducing models to represent the effects of turbulence. To consider flow turbulence and flow viscosity in FLOW-3D, the renormalized group model (RNG), based on K-epsilon (k-ε) is utilized, which applies statistical formulations to calculate the turbulent kinetic energy dissipation rate (Franco et al., 2021). The RNG model is derived from the instantaneous Navier-Stokes equations using a mathematical technique called renormalization group methods. These models provide an analytically derived differential formula for effective viscosity that accounts for a low Reynolds number effect compared with the K-epsilon model which is for a high Reynolds number. The RNG models are more accurate and reliable for a wider class of flows. In recent years, the RNG model has been effectively applied in simulations of landslide surges, the entrainment effects of debris avalanches, dam-break floods, and the runout characteristics of debris flow (Zhang et al., 2021 and Hu et al., 2020). In this work, a debris flow simulation based on the RNG model with various tree trunk patch configurations were executed. This chapter introduces the simulation analysis, covering the model setup, the model geometry, boundary condition types and input data.

3.2 Experimental Study Description

All data performed for this study such as debris flow properties and flume model were taken from experimental data based on Cui et al., (2015). They measured the peak impact pressures of a viscous form of debris flow using a miniature flume experiment. In their experiment, they conducted 27 tests, with Froude number variation between 2.5 and 5.9. Among these 27 tests, three were performed with clean water, while the remaining 24 were conducted with debris flow of varying densities. Subsequently, these results are compared with 155 tests of previous data with Froude number between 0.5 and 10.8. In their experimental set-up, the length of flume was 300 cm, width was 20 cm, and an inclination angle was 15°. Five impact measurement points (five sensors or load cells) S1 to S5 were located at the end of the flume. The diameter of each sensor load was 2 cm diameter and were placed at different vertical depths 0.5 cm, 4.5 cm, 7.5 cm, 10.5 cm, and 13.5 cm from the bottom of the flume as illustrated in Figure 8.

The debris material was flushed down by the gate made of a steel plate which was fixed at the bottom of the upstream tank, which both were installed at the upstream as a debris flow inlet. To analyse the dynamic behaviour of debris flow before impacting, they obtained the dimensionless numbers Froude number (Fr) which associate fluid dynamic properties of debris flow. Therefore, the Fr numbers were introduced by them to describe the differences in flow patterns, and as a dynamic similarity to get scale invariance for the miniaturized flume experiments.

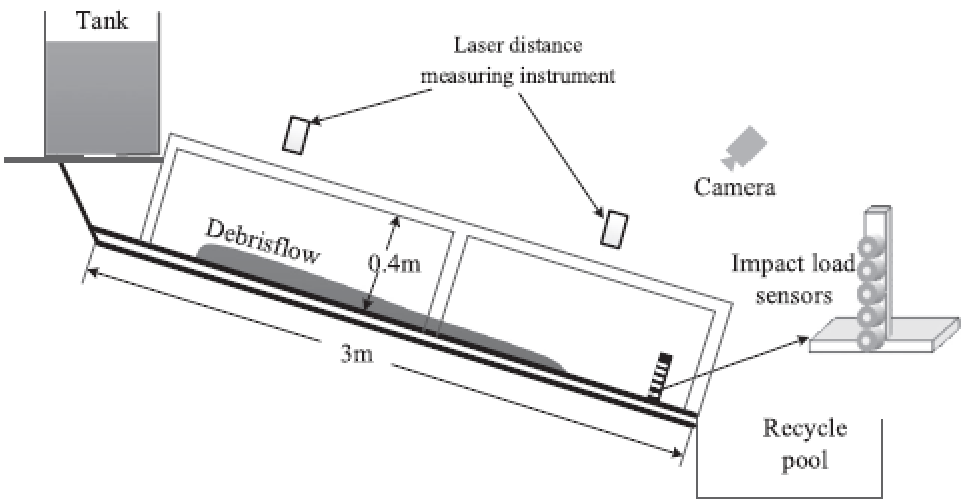

Figure 8: Debris flow experimental model with five impact sensors or load cells at the end of flume (Cui et al., (2015).

3.3 Simulation Setup

Based on experimental study, the length of flume is 300 cm, width is 20 cm, and an inclination angle is 15° as indicated in Figure .12. Five impact measurement points (historical probes) S1 to S5 are located at the end of flume with 2 cm diameter. These points are placed on the wall at 1.5 cm, 4.5 cm, 7.5 cm, 10.5 cm, and 13.5 cm vertical depths from the bottom of the wall. In their experiments, the flow impact pressure processes can be considered into three stages. First, there is a strong impact at the head of the debris flow, followed by a steady impact along the body, and finally, there is a sliding flow at the tail. Due to the lower impact pressure in the debris flow tail, only the initial two steps are considered by them as the impact pressures. Consequently, the impact pressure measured at 10.5 cm and 13.5 cm heights are excluded from their calculations.

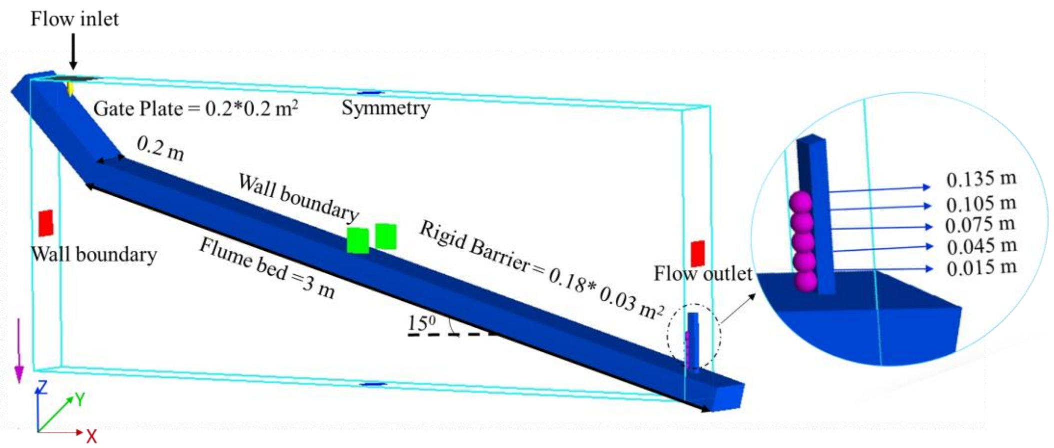

Figure 9: Debris flow simulation model Geometry with various boundary condition types and 5 measurement points (historical probes) on the rigid wall.

3.3.1 Debris Flow Particle Size Distributions

According to data extracted from Cui et al., (2015), the material that are used as an input data for the model contained 2.9% clay, 5.1% silt, 37% sand, and 55% gravel. The fluid density of the debris flow is 2074 (kg/m³) with a water content of 35% and a total volumetric content of 65%. Therefore, the water concentration is taken as 724.9 kg/m³, and the sediment concentration is 1348 kg/m³ in the simulation model. Consequently, the volumetric concentrations for clay, silt, sand, and gravel are 39.1 (kg/m³), 68.7 (kg/m³), 498.8 (kg/m³), and 741.4 (kg/m³), respectively as illustrated in Table 3. The cumulative percent passing of grain size, represented in Figure 10, are employed as input data for defining debris flow particle size. As shown in the graph, the maximum particle size is 20 mm. To achieve the same material contents of the different grain size diameters that align with experimental data, four different gravel contents of 6%, 5%, 29%, and 15%, with diameters of 16 mm, 12 mm, 8 mm, and 3 mm are applied in the model respectively. additionally, four different sand contents of 11%, 9%, 14%, and 3%, with diameters of 1.75 mm, 0.9 mm, 0.375 mm, and 0.11 mm are assigned respectively. Furthermore, for the silt and clay contents, percentages of 5.1% and 2.9% with diameters of 0.04 mm and 0.002 mm are respectively applied in the model.

Table 3: volumetric consideration of particle contents

	Particle Contents %	**Particle Diameter (mm)**	**Volumetric Concentrations**
clay	2.9	0.001- 0.005	39.0949
silt	5.1	0.005 – 0.1	68.7531
sand	37	0.1 – 2.36	498.797
gravel	55	2.36 - 20	741.455

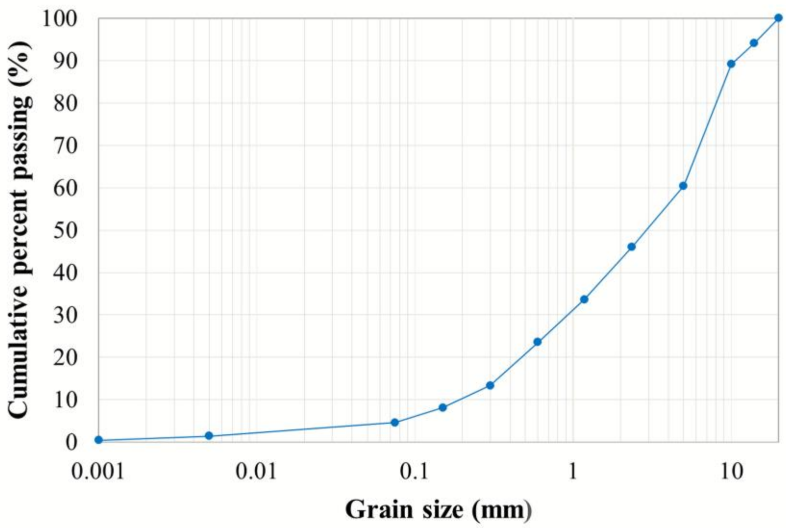

Figure 10: Debris flow cumulative grain size distribution

3.3.2 Boundary Condition for Model Validation

To achieve meaningful and reliable findings, boundary condition type is essential for defining the simulation environment accurately. Also, boundary types are assigned to specify the limits of the domain, physical space and conducted simulation conditions. Meanwhile, within the simulation domain one can clearly define how fluid enters, exits, and interacts with surfaces. A wall boundary type is assigned to X_{min}, Y_{min}, Y_{max} and Z_{min} since there are no outflows in that particular regions. On the other hand, outlet flow is applied at X_{max}, and a symmetry boundary type is assigned at Z_{max} as illustrated in Figure 9.

3.3.3 Initial Conditions for Model Validation

As part of setting up the model, all material contents are applied in the fluid initialization, and material diameters are specified in the physics of the model as the sediments scour window. To match the experimental conditions carried out by Cui et al., (2015), the debris flow volume inside the tank was set to $1 \times 1 \times 0.23$ m^3. Using the equation $v = \sqrt{2gh}$, the velocity was calculated to be 2.12 m/s. Hence, with a drain time of 3-4 seconds, the drain area was determined to be 0.04 m^2 through trial and error.

In the mass momentum source window, the debris flow geometry and properties are performed, including details such as the shape (a square with dimensions of 20 x 20 cm^2), flow direction (oriented along the -z axis), and rotation (a 180-degree rotation in the y-direction). This configuration is evident in Figure 9, which represents the flow geometry as an inlet flow. To achieve a same debris flow discharge in accordance with the experimental results, the flow rate is scheduled as tabulated in Table 4. The debris flow properties, such as dynamic viscosity, and all the input data are provided from the experimental study of Cui et al., (2015). Those which were used in this study for the simulation model, are listed in Table 5.

Table 4: Debris flow discharge timetable for simulation analyses

Time (sec)	0 – 2.5	2.5 – 3.1	3.1 – 4	4 – 5	5 – 6	6 – 8
Q (m^3/s)	0.11	0.05	0.01	0.005	0.001	0.0001

3.3.4 Generation Mesh for Validated Model

In computational fluid dynamic simulations, the mesh provides the necessary framework for ensuring numerical stability and accuracy, discretizing the fluid domain, and optimizing computational resources. In order to obtain good mesh quality in Flow–3D, the maximum aspect ratio within a single cell should be less than 3 and the maximum adjacent cell size ratio should be less than 1.25 and additionally the maximum inter-block cell size ratio should be less than 2. Considering these factors, a uniform Cartesian mesh with finite meshes of 0.003 m cell sizes was utilized for the entire model of the preset work. The total number of real cells for all mesh blocks is 11474000.

Table 5: Debris flow simulation input variable

Parameters	Value
Specific gravity (Gs)	2.65
Flume inclination angle (degrees)	15
Average grain diameter d_{50} (m)	0.0027
Dynamic Viscosity (pa s)	0.096
Yield stress (Pa)	30.32
Fluid viscosity (kg/m/s)	0.001
Debris flow fluid density (kg/m^3)	2074
Friction angle (degrees)	32
Water concentration	0.35
Sediment volume concentration	0.65
Total debris flow volume (m^3)	0.23

3.4 Validation of Simulations with Experimental Results.

The validation of debris flow simulation analysis conducted here is classified into different simulations, with and without sediment particle (clean water) distribution and are validated using the experimental results of Cui et al., (2015). Based on the simulation and experimental results, both clean water and debris flow impact pressures do not reach point S5 in terms of height. This evidence is clear in Figure 11 and Figure 12. Therefore, in the Figure 15, S5 is a straight line at pressure = 0 (Pa), parallel to x axes for both models. For clean water, the peak pressure or damaged area is generated in S1 and concentrated at 3.5 cm from the flume bed for the first impact and then ascends to 6 cm, as illustrated in Figure 11. For debris flow, it occures in S1 and rises to 4.5 cm for the first impact and then ascends to 7.5 cm Figure 12. The velocity of the clean water is estimated as 4.9 (m/s), Froude number is 5.2 and the maximum impact pressure is 12.6 (kPa), Figure 11. Using the input parameters provided in Table 5 for water with sediment particles, the determined results include a debris flow velocity of

4.1 (m/s), a Froude number of 3.8, and a maximum impact pressure of 31.9 (kPa), as illustrated in Figure 12.

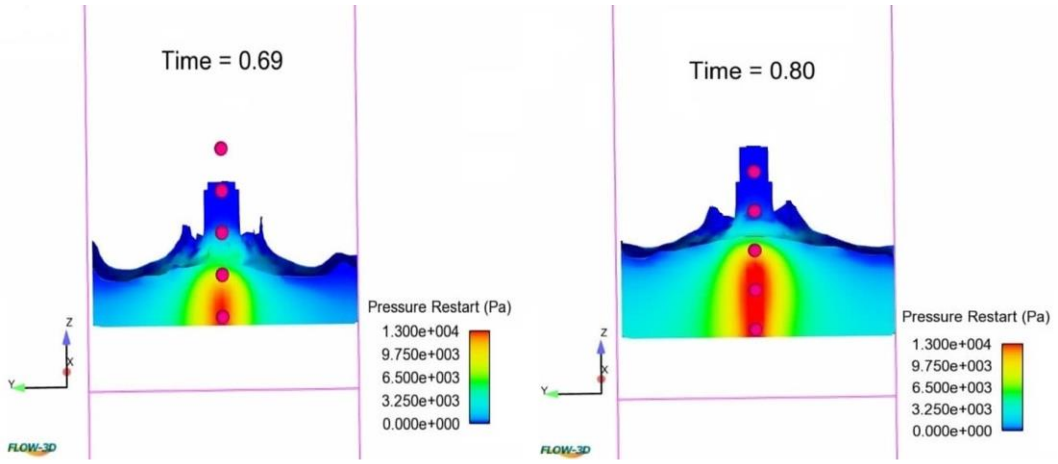

Figure 11: The pressure distributions in the 5 measurement points on the rigid wall for clean water model based on experimental data

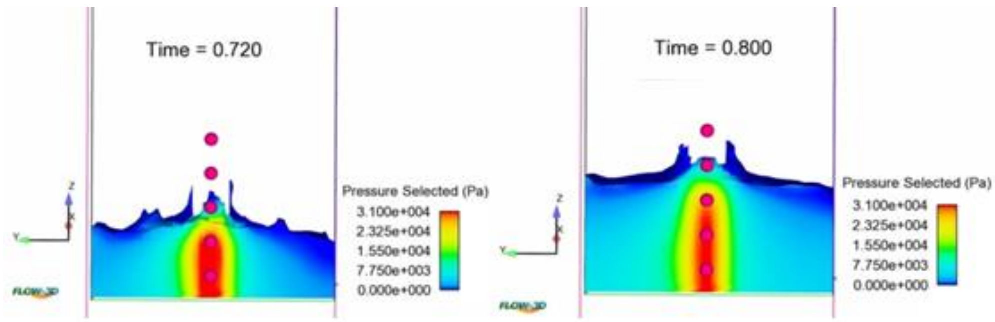

Figure 12: The pressure distributions in the 5 measurement points on the rigid wall for debris flow model based on experimental data

The clean water impact pressure at the first measurement point, S1, is sustained for about 5-6 seconds, while at other points, it is sustained for 3-4 seconds as illustrated in Figure 13 section (a). Hence, the debris flow impact pressure at the first measurement points is sustained for about 6-7 seconds, Figure 13 section (b).

Figure 14 section (a) and (b) show the comparison between experimental data and simulation results in three different measurement point heights (1.5 cm, 4.5 cm, and

7.5 cm) from flume bed. In clean water, the percentage error of the simulated analyses are less than 2% for the first and second heights, and below 5% for the third height as compared with experimental results. Similarly, in debris flow the percentage error simulated analyses at each height are less than 2% of experimental results. As a result, the (MSE) is 0.09 for clean water and 0.13 for debris flow. Therefore, the findings are in good agreement with the experimental observations.

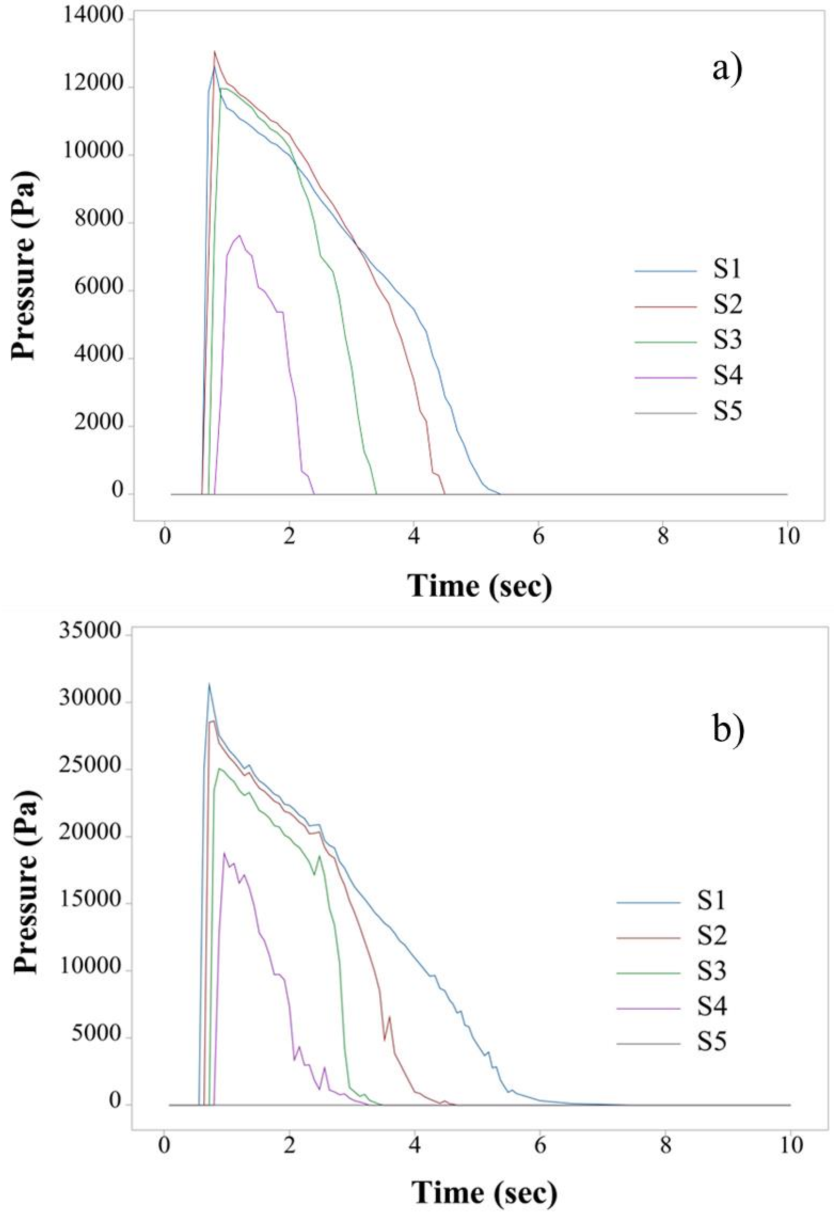

Figure 13: Impact pressure determination for different measurement points (1.5 cm, 4.5 cm, and 7.5 cm above the flume bed) that placed at different height, (a) clean water, (b) debris flow

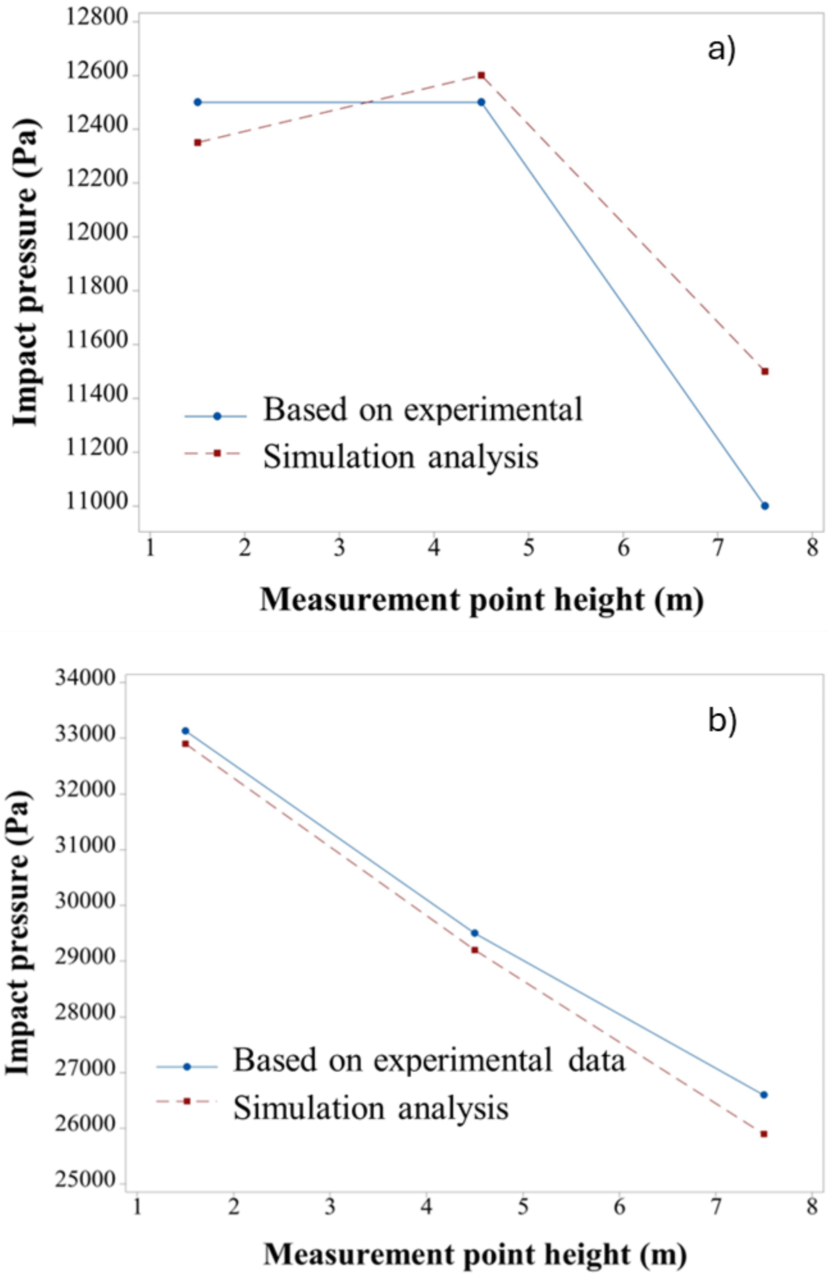

Figure 14: validation of experimental data based on simulation analysis for different measurement points (1.5 cm, 4.5 cm, and 7.5 cm above the flume bed) that were placed at different height, for a) Clean water and b) Debris flow

The analytical results obtained from Eq.25 are validated by using experimental data from Cui et al., (2015). In their experiment, they conducted a total of 27 tests, with a Froude number variation between 2.5 and 5.9. Subsequently, these results are compared with 155 tests of previous data with Froude number between 0.5 and 10.8 by Hübl and Holzinger, (2003); Tiberghien et al., (2007) and Scheidl et al., (2012) and field experiment analyses by Costa, (1984) and Zhang and Yuan, (1985). In this study, subcritical flow data (Fr<1) have been removed from the calculation. The result of the regression hydrodynamic model derived by Cui et al., (2015) is expressed in Eq.11 and is given in Figure 15:

$$\frac{P_{dmax}}{\rho\, u^2} = 5.3\, Fr^{-1.5} \qquad (32)$$

The impact pressure analysis data from Cui et al., (2015) are inserted into Eq. 26 and the results are plotted on the power line with regression error square (R^2) of 0.95 to show that the results are matching with the previous studies as shown in Figure 15.

Since the data used for validation is being extracted from Cui et al., (2015) research, and since the Froude number ranges from 2.5 to 5.9, data outside these ranges were removed from the Figure 15. These changes allow for a clearer observation of the variation in the drag coefficient in the new graph illustrated in Figure 16. In Table 6, the dynamic empirical coefficient in the first column is calculated based on the experimental results as a function of the experimental Froude number. The second column is obtained from analytical results by inserting Eq. 25 into Eq. 2 as a function of the experimental Froude number. In addition, the last column is calculated for a range of Froude numbers between 1 and 10. Based on these ranges the dimensionless empirical coefficient, α is analytically calculated to be in the range of 0.42 and 1.86 as shown in Table 6.

Table 6: Drag force empirical coefficient (α) as the function of the Froude number based on experimental and analytical results

Fr Based on experiments conducted by (Cui et al., (2015)	**α Based on Analytical Results in this thesis**	**α Based on experiments conducted by (Cui et al., (2015)**	**Fr Based on experiments used by Cui et al., (2015) and conducted by other researchers**	**α Based on Eq. (31)**
4.50	0.59	0.60	1	5.30
2.60	1.47	1.41	1.2	4.03
2.50	1.65	1.61	1.5	2.88
5.20	0.42	0.48	1.8	2.19
5.60	0.46	0.47	2	1.87
2.36	1.86	1.75	2.2	1.62
3.71	0.95	0.93	2.5	1.34
2.80	1.48	1.49	3	1.02
4.33	0.56	0.48	3.2	0.93
3.90	0.83	0.74	3.5	0.81
4.80	0.68	0.67	4	0.66
4.11	0.78	0.80	4.2	0.62
4.10	0.78	0.84	4.5	0.56
4.40	0.75	0.75	5	0.47
4.50	0.76	0.85	5.5	0.41
4.40	0.81	0.82	6	0.36
4.11	0.70	0.75	6.5	0.32
4.50	0.65	0.66	7	0.29
4.50	0.71	0.73	7.5	0.26
4.11	0.60	0.57	8	0.23
4.80	0.61	0.69	8.5	0.21
4.33	0.66	0.72	9	0.20
4.59	0.51	0.52	9.5	0.18
			9.7	0.18
			10.8	0.17

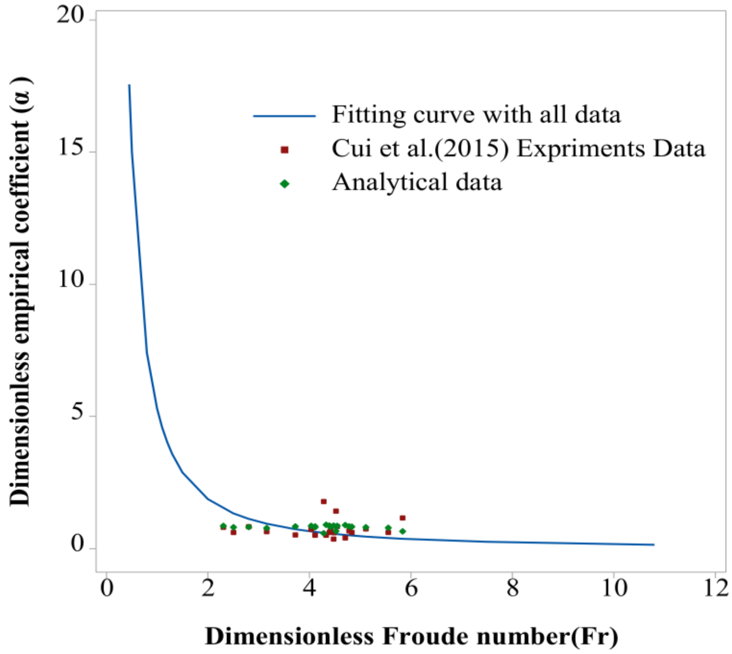

Figure 15: Analytical and experimental relationships between empirical coefficients and Froude number

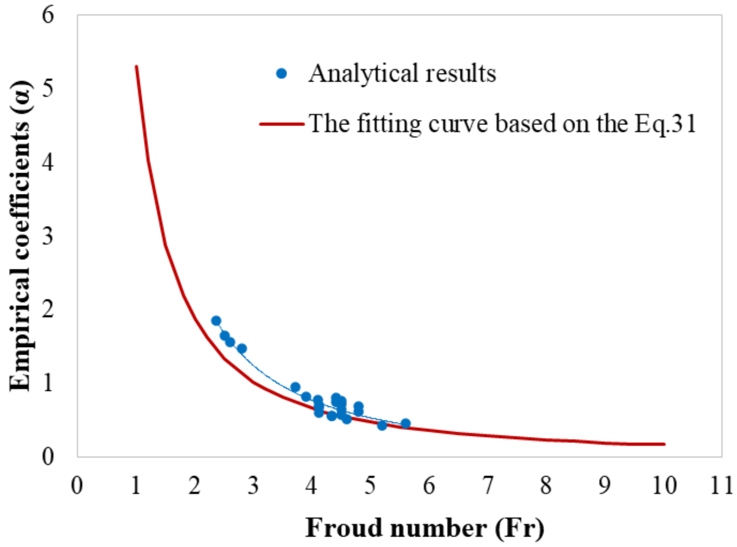

Figure 16: Relationship between empirical coefficients and Froude number based on Analytical and experimental results for Fr between 2.5to 5.9

3.5 Numerical Model Description with Tree Trunk Patches

Process response simulations between tree trunk patches and debris flow require the identification of three-dimensional flow tracking and complex geometry. In the present work, the flume size is identical to that in experimental studies. To specify the impact pressure distribution on the rigid wall, the size of the wall was enlarged and the measurement points were increased.

To calculate the maximum impact pressure of debris flow on a rigid vertical wall, tree trunk patches, after passing through different configurations, have been used. For the development of effective measures, two different configurations are simulated. In one simulation, the number of rows of tree trunks increased upstream, whereas in the second configurations, the density of tree trunks increased within a predefined area.

3.5.1 The Geometry and Boundary Condition of Numerical Analysis

In analysing debris flow impact force, crucial factors are selected with the reference to Cui et al., (2015) studies. All initial condition processes, particle size distribution, and input data listed in Table 5 to those in the validation section are identical for the simulated model in the present work. The simulated flume is 300 cm long and 20 cm wide with an inclination angle 15° which is exhibited in Figure 17. The 3 cm thick wall is placed at the end of the flume. The height of wall is 25 cm, and its width is 12 cm. The debris material is flushed down by gate with 20x20 cm^2 area, placed at 50 cm from the top of the flume as a flow inlet. To measure the debris flow impact pressure, 18 measurement points (historical probes) with 2 cm diameter are applied and positioned on the wall at different vertical heights: 1.5 cm, 4.5 cm, 7.5 cm, 10.5 cm, 13.5 cm, and 16.5 cm from the bottom of the rigid wall.

The boundary conditions for the entire model are same as those mentioned in the validation section. For vegetated areas, symmetry boundary conditions were assigned to X_{min} and Z_{max}, wall conditions were applied to Y_{min}, Y_{max}, and Z_{min}, and outflow conditions were assigned to X_{max} as depicted in Figure 17.

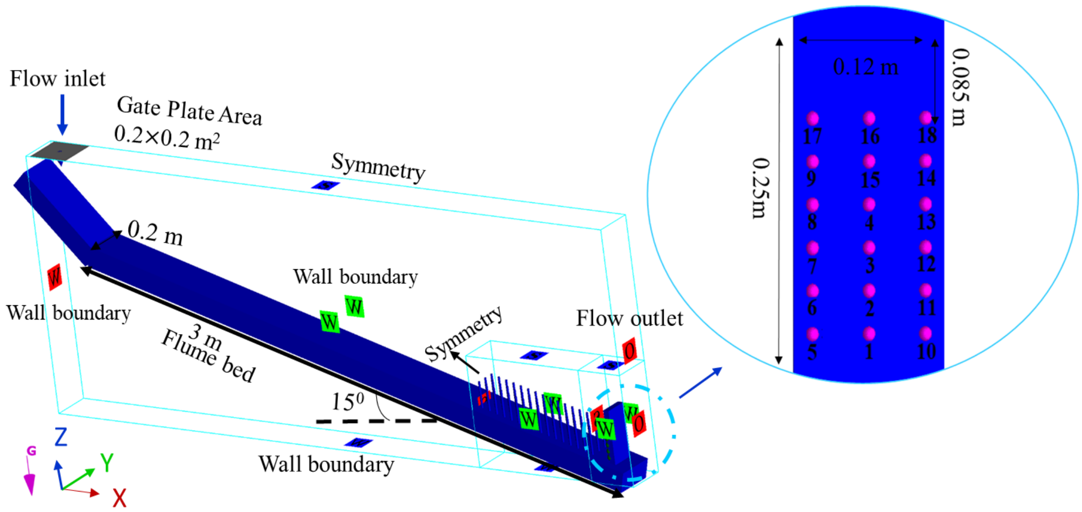

Figure 17: Debris flow simulation model Geometry with various boundary condition types and 18 measurement points (historical probes) on the rigid wall.

3.5.2 Mesh Generation of Fluid Domain

To minimize memory usage and runtime of the model the cartesian meshes are generated using the nested multi-block grid mesh in flow 3D. Several mesh tests are performed in the simulation model to ensure that the numerical solution remains consistent and does not significantly change with different grid settings. Due to dealing with elements of different sizes, both uniform and non-uniform Cartesian mesh sizes are defined in the geometry. Uniform Cartesian mesh cell size of 0.005 m is used as finite meshes for the entire area. To improve mesh size precision for the tree trunk area and rigid wall, two different non-uniform block meshes are employed as illustrated in the Figure 18.

In block (a), the cell counts 100 and 200 are applied in both the y and z directions for all group models A and B respectively. However, due to different configurations in the x direction for group models A and B, the cell counts of 200 are allocated to the B6 model, longest tree truck rows, in the x direction which have indicated the average mesh sizes of 0.002 m. To provide uniform precision for all group models A and B, a ratio of 308 cell counts per meter is applied and detailed in Table *7*. Furthermore, in block (b), cell counts of 100 are assigned in the x, y, and z directions for all group models. The total number of real cells for all mesh blocks is 11,474,000. In order to increase the efficacy of results in FLOW-3D, the size ratio between the adjacent cells should be close to unity as much as possible and must not exceed 1.25. Moreover, aspect ratios of the cells should also approximate unity as much as possible, and not exceed 3.0 because cell aspect ratios exceeding 3.0 can cause pressure iteration problems. Furthermore, all degrees of freedom for cells at all the sides (x, y and z) and bottom are fixed as shown as mesh planes in Figure 18.

Table 7: Number of cell counts per meter for different tree trunk configurations

Group Model	**A1**	**A2**	**A3**	**A4**	**A5**	**A6**
Cell Counts for Block (a) per (m)	28	28	28	28	28	28
Group Model	**B1**	**B2**	**B3**	**B4**	**B5**	**B6**
Cell Counts for Block (a) per (m)	3	28	53	89	139	200

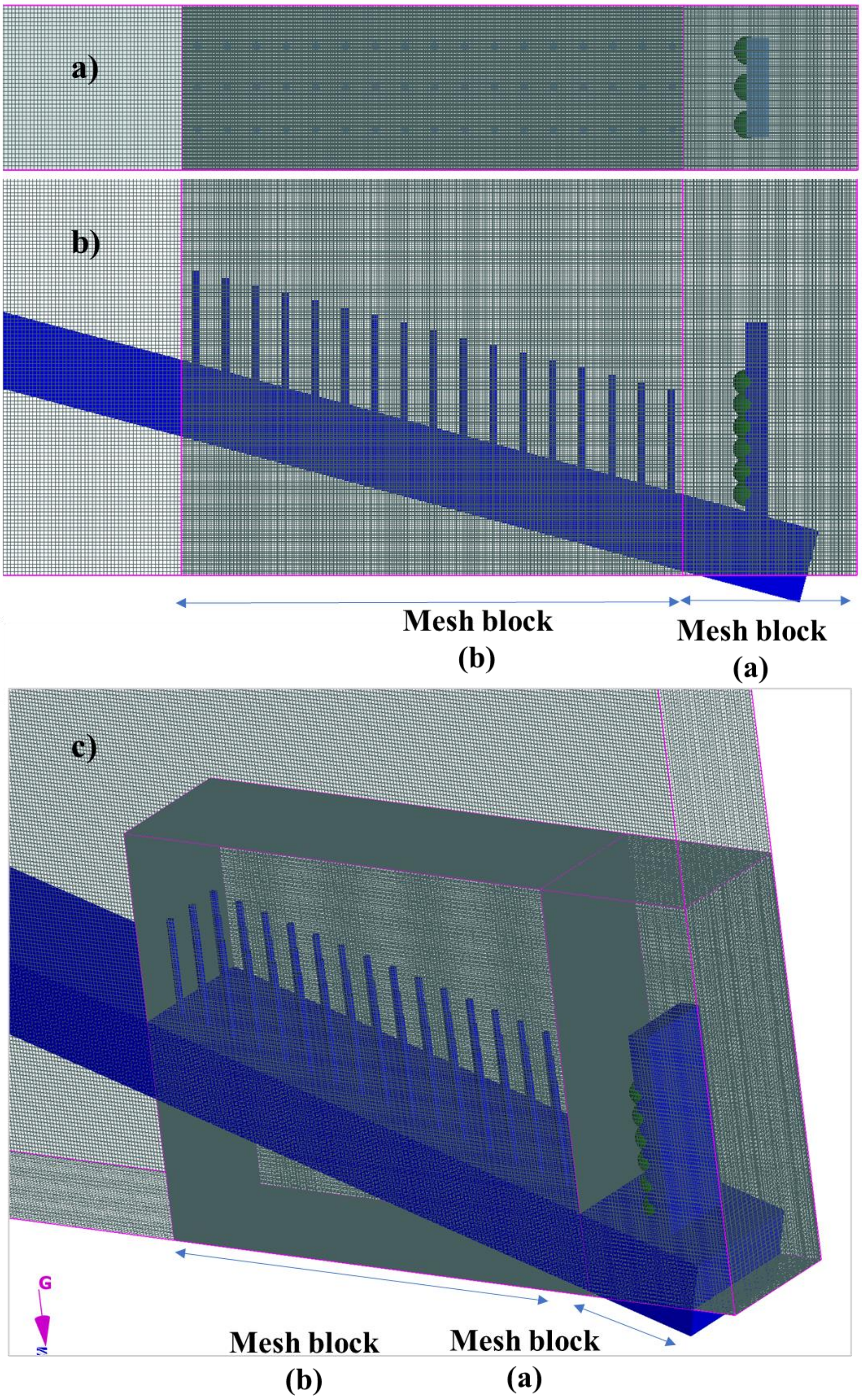

Figure 18: Computational mesh grid of the simulated model in the control volume with two different adding mesh block (a) and (b): section a) top view, section b) side view and section c) 3D view.

By considering all the above features, the simulation ran for all groups in models A and B, and the results were compared by increasing tree trunk numbers and with those obtained without mitigation methods. The findings are described in Chapter 4 and 5.

Chapter 4

SIMULATION AND ANALYTICAL RESULTS

4.1 Overview

In this chapter, all findings are compared by increasing tree trunk numbers and with those obtained without this mitigation method. Additionally, the results of impact force per unit meter are calculated and compared with simulation analyses. By considering these findings, a new dynamic coefficient (α) as a function of the Froude number using tree trunk patches is estimated. Additionally, a new expression for the drag force coefficient for different tree trunk configurations is devised.

4.2 Impact Pressure Without Tree Trunk Patches

Before comparing the maximum impact pressure for both group model configurations, simulations were run without stem or tree trunk patches. This also help to demonstrate effective mitigation methods like tree trunks in reducing impact pressure. The momentum flux leaving the control volume of the vegetated area generates pressure on the vertical wall. Figure 19 depicts the impact pressure over the wall at different measurement points. It can be noted that the maximum impact pressure is distributed between the first four rows up to a depth of 10.5 cm from the bottom. It is clear from the Figure that the peak impact pressure is concentrated in the middle area from the wall bottom which was obtained at 44.3 kPa. Figure 20 indicates the graphical variation of impact pressure distribution curves for measurement points S1 to S12 as the function of time. Figure 23 is illustrated by minimizing the measurement points (historical probes) and showing only the 12 measurement points to display pressure variation clearly. It is clear from Figure . 23 that the impact pressure processes are sustained for about 6 -7 seconds.

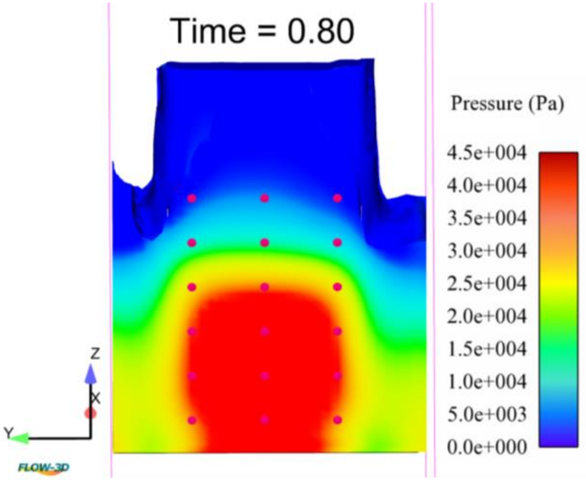

Figure 19: The pressure distributions in the 12 measurement points (S1 to S12) on the rigid wall for without stems models

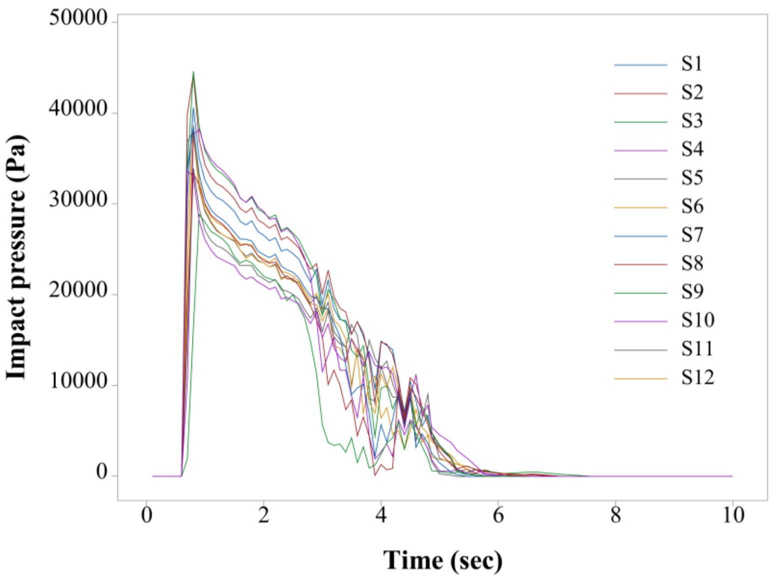

Figure 20: Debris flow impact Pressures at measurement points (S1 to S112) were placed at different depths for model without stems.

4.3 All Forces that Act on the Vegetated Area within the Control Volume

All forces per unit meter were measured with specified density, tree trunk diameters, and distances using Eq. 27, which was obtained in Chapter 2. The results are shown in Table *8*. The momentum flux leaving the control volume of the vegetated area generates pressure on the vertical wall. Eighteen measuring points (S1 to S18) have been used to assess impact pressure on the wall. Each point was arranged to have a 3 cm vertical and 4 cm horizontal distance from each other. Eighteen measuring points (S1 to S18) have been determined to assess pressure on the wall at 3 cm vertical and 4 cm horizontal distance from each other. As is clear in Table 8, by increasing the tree trunk patches, the outgoing momentum flux is reduced. For example, in group model A, the reduction is from 44.1 kN/m for model A1 to 13.7 kN/m for model A6. Similarly, in group model B, the reduction is from 39.6 kN/m to 29.5 kN/m.

The arriving time of peak impact pressures based on the effect of tree trunks is shown in Table 8, where peak impact pressure arrival times are changed from 0.76 to 1.2 seconds for group model A and from 0.76 to 0.9 seconds for group model B. In addition, as the number of tree trunks increases for both group models A and B within the control volume, the flow velocity is minimized, and consequently, the debris flow depth increases, as illustrated in Table 8. These changes are more pronounced in group model A, where the depths change from 14 cm to 25 cm.

Figure 21 and Figure 22 indicate the graphical variation of impact pressure between S1 and S18 for both A4 and B5 models as a function of time. It can be noted that, by the increase of tree trunks against the debris flow path, the duration of the rigid wall impact pressure also increases. For instance, approximately 9 to 10 seconds are estimated to be sustained for A4 and 8 to 9 seconds for B5 as indicated in Figure 21 and Figure 22.

Table 8: Analytical results for both group models A and B

Group models A									
Solid volume fraction (??) %	Peak Impact arriving Time (sec)	Depth H_{out} (cm)	Velocity u (m/s)	Froude number	M_{in} kN/m)	F_D (kN/m)	F_g (kN/m)	F_p (kN/m)	F_{bs} (kN/m)
1	0.76	14	4.6	3.93	47.8	2.2	0.60	0.62	1.45
1.96	0.8	16.5	3.9	3.06	47.8	20.8	7.10	0.74	1.71
3.9	0.8	15.2	4.2	3.48	47.8	8.7	0.68	0.70	1.64
7.8	1	18.9	3.4	2.49	47.8	29.1	8.15	0.84	1.97
15.7	1	17.2	3.7	2.87	47.8	23.6	7.41	0.77	1.79
31.4	1.2	25.4	2.5	1.61	47.8	41.5	10.90	1.13	2.63
Group models B									
Vegetated length parameter ø	Peak Impact Arriving Time (sec)	Depth H_{out} (cm)	Velocity u (m/s)	Froude number	M_{in} (kN/m)	F_D (kN/m)	F_g (kN/m)	F_p (kN/m)	F_{bs} (kN/m)
0.04	0.76	14.7	4.4	3.6	47.8	6.5	0.70	0.73	1.69
0.12	0.8	15.2	4.2	3.5	47.8	8.7	0.68	0.70	1.64
0.2	0.9	16.1	4.0	3.2	47.8	12.9	0.72	0.75	1.74
0.31	0.9	17	3.8	2.9	47.8	16.2	0.76	0.79	1.84
0.47	0.9	17.1	3.8	2.9	47.8	16.4	0.77	0.79	1.85
0.67	0.9	17.1	3.8	2.9	47.8	16.4	0.77	0.79	1.85

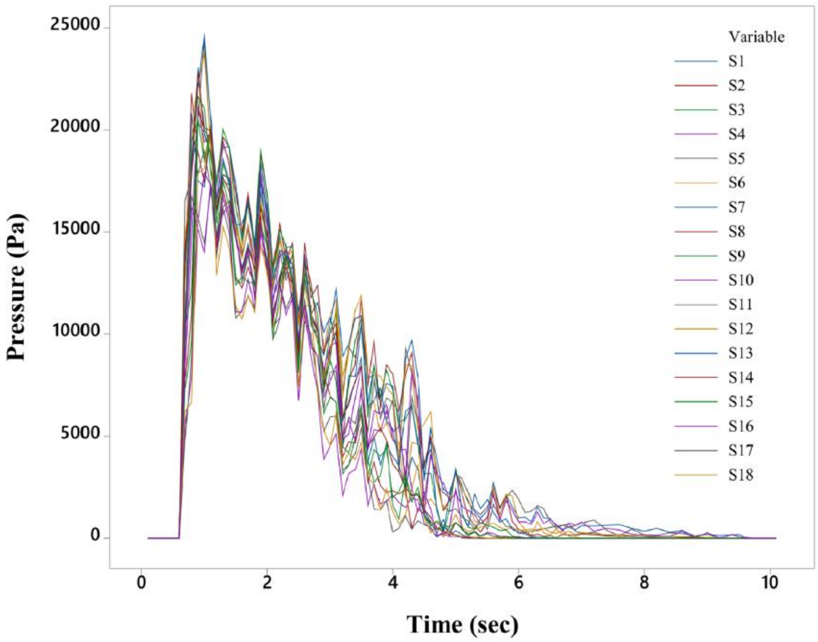

Figure 21: Debris flow impact Pressures at all measurement points (S1 to S18) placed at different depths for model A4

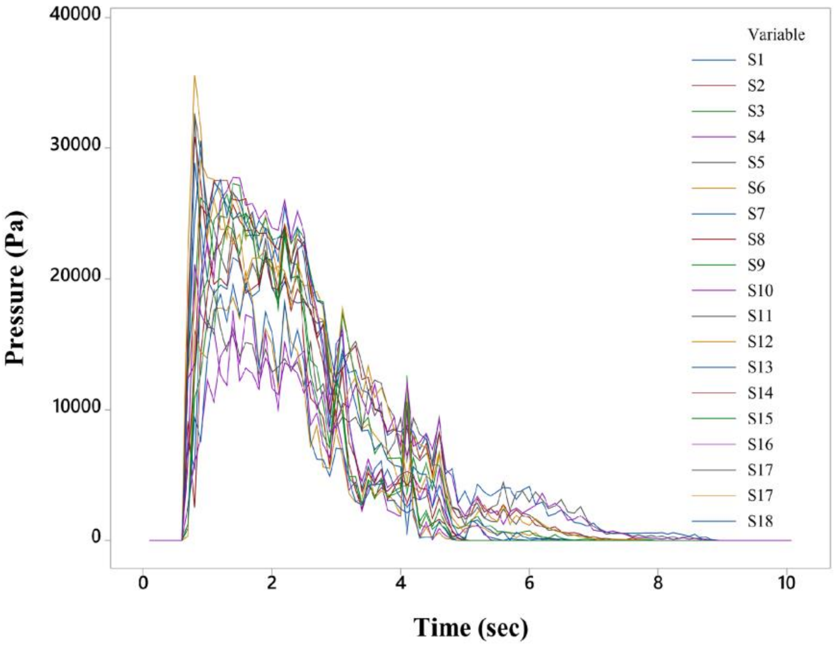

Figure 22: Debris flow impact Pressures at all measurement points (S1 to S18) placed at different depths for model B5

4.4 Impact Pressure on Vertical Rigid Wall by Using Tree Trunk Patches

Twelve model tests were performed with different tree trunk arrays in linear, rectilinear, and vegetated lengths. Figure 23 shows the tree trunk patch configurations as examples for group models A6 and B6. Each point was arranged to have a depth of 1.5 cm above the bottom and a vertical distance of 3 cm and a horizontal distance of 4 cm from each other. The simulation ran for all groups in models A and B, and the results for all 18 measurement points were tabulated at Table 9. The damage or peak pressure areas are colored red in the table. This indicates that each group model has a different peak pressure area due to the different configurations of tree trunk patches. In the A1 model, the peak impact pressure is concentrated in the middle area between the S2 and S3 measurement points. However, as the tree trunk density increases, the peak impact pressure reduces while damaged area ascends.

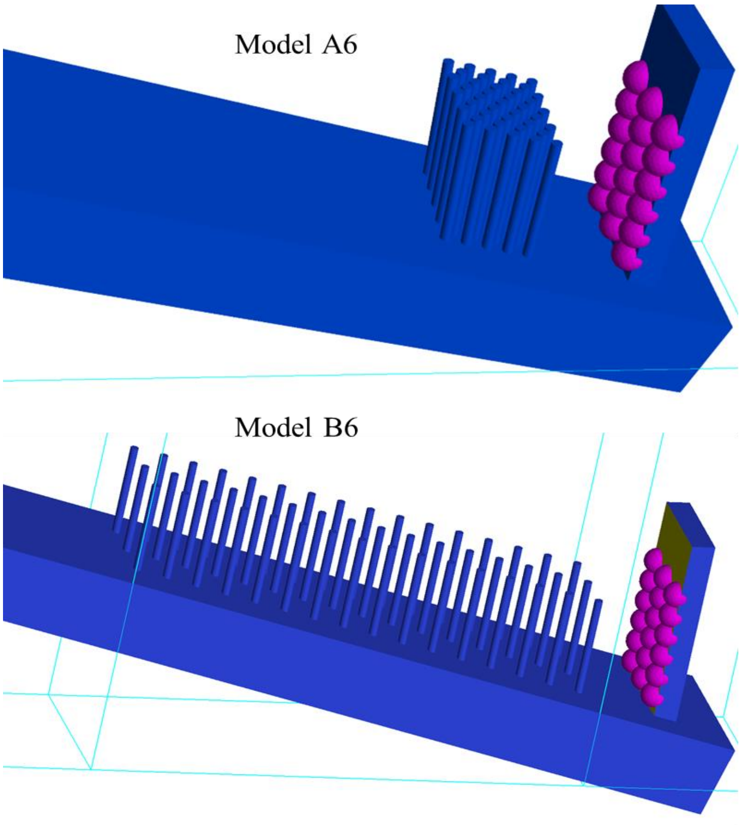

Figure 23: Arranging the tree trunk patches for both models A6 and B6

Figure 24 and Figure 25 exhibit the front view impact pressure distribution along the rigid wall models A and B. It can be seen that for group model A (linear and rectilinear), the maximum impact pressure is concentrated in between 4.5 to 10.5 cm above the floor. As the solid volume fraction increased, independent of linear or rectilinear configurations of tree trunks, the effect of impact pressure decreased. When the maximum impact pressures at A1 are compared with the max impact pressures at A6, a reduction of 67.3%, 69.5% and, 70% in maximum pressures are observed at S4, S3, and S2, respectively. Another important observation is the increase in the depth of flow in parallel to the increase of solid volume fraction. Due to the velocity retarding effect (drag force effect) of the tree trunks, the velocity of debris flow experienced a reduction of 4.6 to 2.5 (m/sec) along the flow direction. Based on the principles of continuity, a decrease in velocity increases the flow area, which in turn increases the depth of the debris flow. The depth ascended from 14 cm to 25 cm. Consequently, the reduction in the velocity did not change the regime of the flow and the supercritical flow properties dominate the flow. However, as seen in Figure 24, a considerable increase of maximum impact pressures at the top of the wall is observed due to the rise in the debris flow depth. The retarding effect of tree trunks on the occurrence time of peak impact pressures is given in Figure 24 indicating 58% shift in the occurrence time of peak impact pressures.

The simulation for model B configurations clearly depicted the effect of drag on the debris flow. The in-line ordered trunks generated an easy path for debris flow to reach the wall thus, maximum impact pressures are observed due to these flows. On the other hand, as the vegetated length parameter increased the pressure dropped in the projection of tree trunks. The peak pressures on the wall are around 39 (kPa) in model B1 simulations and it dropped to 29 (kPa) in B6 simulations. Approximately, 34% reduction in peak impact pressure is not as good as the results achieved in Model A simulations. Significant reduction in velocity of debris flow is not perceived as in the case of model A simulations. As $\emptyset$ (the vegetated-length-parameter) enlarges from 0.04 to 0.67, a slight decrease in debris flow velocity is monitored (from 4.4 to 3.8 (m/s)). Meanwhile, the flow depth increased from 15 cm to 17 cm. As a consequence, the necessary time required to monitor the occurrence of peak impact pressures on the wall did not very much, Figure 25.

Table 9: Numerical results for both group models A and B

Flow model	Row	P (kP)	P (kP)	P (kP)	Flow model	Row	P (kP)	P (kP)	P (kP)	Flow model	Row	P (kP)	P (kP)	P (kP)
A1	6	2.8	4.88	2.7	**A2**	6	9.7	15.7	9.9	**A3**	6	27.3	20.2	27.5
	5	15.9	28.7	15.8		5	24.68	23.5	24.3		5	34.8	21.3	34.9
	4	30.7	42.5	29.9		4	28.57	20.28	28.3		4	37.4	26.5	37.4
	3	35.8	44.1	34.6		3	31.5	22.8	31.65		3	35.3	28.9	35.4
	2	35.8	44.1	35.8		2	31.3	18.9	30.23		2	24.3	28.2	24.2
	1	32.9	40.7	32.8		1	19.01	19.63	19.08		1	20.2	20.9	20.2
A4	6	20.5	19.01	20.34	**A5**	6	20.8	24.3	20.8	**A6**	6	3.92	6.19	4.96
	5	21.62	20.3	21.09		5	22.1	28.2	22.1		5	8.25	12.7	8.21
	4	24.85	21.07	24.84		4	23.2	29	23.4		4	8.16	13.4	8.15
	3	22.88	20.5	22.86		3	23.5	29.1	23.5		3	8.44	13.4	8.48
	2	22.2	18.5	20.58		2	22	28.9	22		2	7.88	12.3	7.68
	1	15.66	17.5	15.13		1	18.7	24.7	18.7		1	7.48	10.7	7.24
B1	6	1.4	1.6	1.4	**B2**	6	27.3	20.2	27.5	**B3**	6	25.2	28.5	25.2
	5	12.7	12.5	12.7		5	34.8	21.3	34.9		5	28.2	22.7	28.1
	4	32.1	25.3	32.3		4	37.4	26.5	37.4		4	30.7	26.1	30.7
	3	38.8	25.5	38.9		3	35.3	28.9	35.4		3	33.1	28.6	33.1
	2	39.6	29.6	39.6		2	24.3	28.2	24.2		2	30.1	28.2	31.57
	1	34.7	35.4	34.6		1	20.2	20.9	20.2		1	22.02	25.4	22.4
B4	6	11.8	12.3	11.8	**B5**	6	7.5	12.7	7.8	**B6**	6	5.5	6.5	5.7
	5	18.9	22.9	18.1		5	15.5	14.5	14.3		5	12.7	8.73	12.4
	4	29.7	23.7	29.8		4	29.5	19.11	29.5		4	29.7	18.5	29.7
	3	28.7	26.9	28.8		3	29.2	26.1	29.2		3	29.5	26.2	29.5
	2	24.4	26	24.3		2	29.52	25.3	29.59		2	29.4	25.3	29.5
	1	18.7	26.3	18.5		1	22.27	24.07	22.5		1	21.2	24.5	20.5

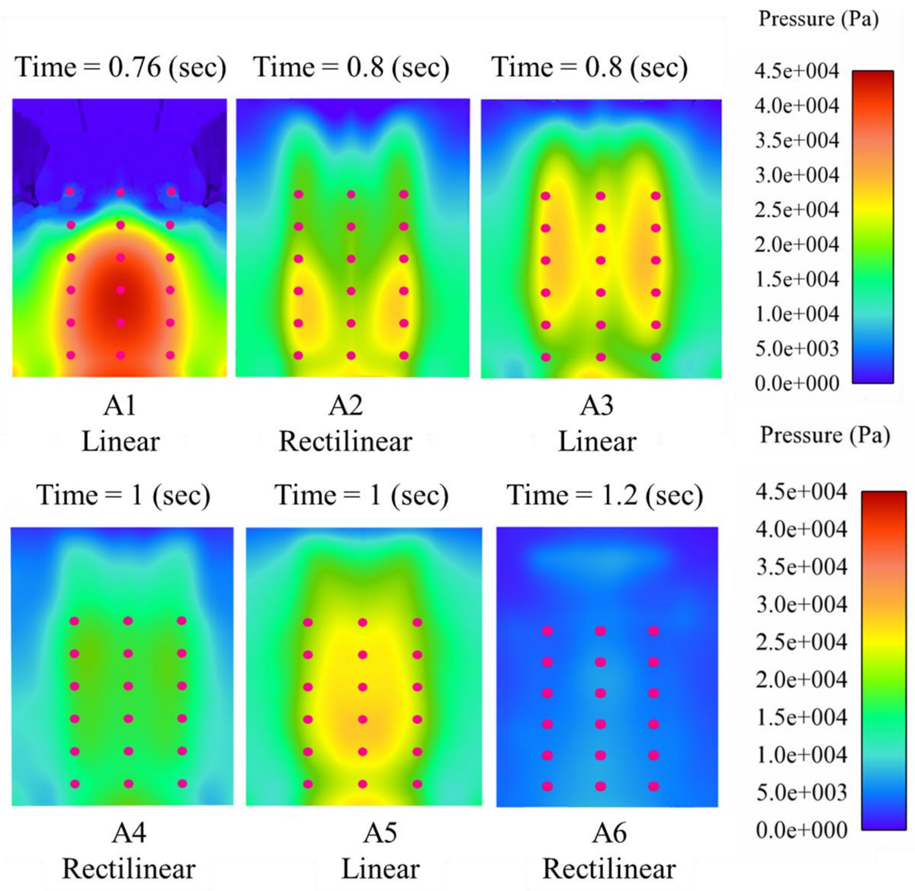

Figure 24: The pressure distributions in the 18 measurement points on the rigid wall for group models A with various tree trunks density (1.3, 2.84, 11.1, 16 and 44.4, m^{-1}) and solid volume fractions (0.98, 1.96, 3.9, 7.8, 15.7 and 31.4, %).

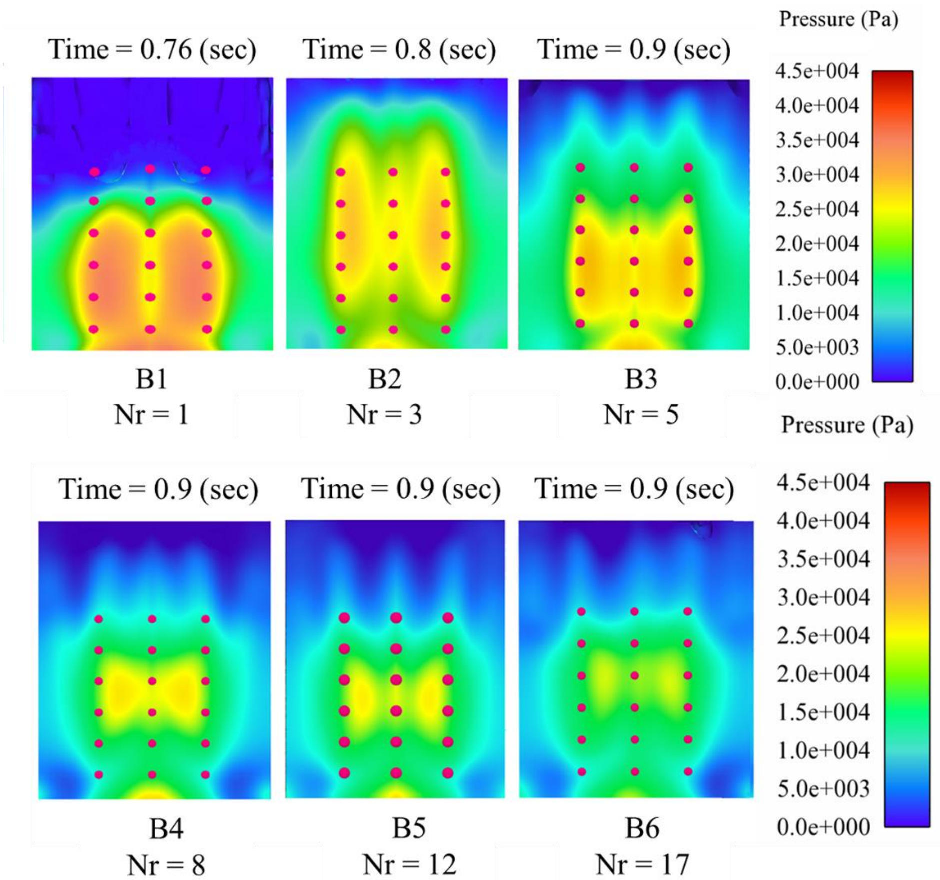

Figure 25: The Pressure distributions in the 18 measurement points on the rigid wall for group models B with various Vegetated length parameter, Ø (0.04, 0.12, 0.2, 0.31, 0.47 and 0.67)

4.5 Normalized Drag Coefficient

There are several research studies that define the drag force and coefficient based on various assumptions. Some of them ignore the dominant effect of the Reynolds number (Riazi and Türker, 2019) while some assume that the drag force is linearly changing with flow velocity (Türker and Valyrakis, 2021), implement the drag force concept on linearly and randomly distributed trees based on using a quadratic drag law and concluded that the variation in drag force increases as the density of trees increased. For the analyses of drag coefficient along an individual tree trunk, the drag force equation (Eq. 27) can be given as:

$$C_D = \frac{2F_D}{\bar{\rho}u^2dh} \quad (33)$$

in which u and h are debris flow velocity and depth, respectively. Based on the data given in Table *8*, under the assumption that debris flow velocity, density and tree trunk area are constant at the entrance of control volume, the magnitude of C_D will vary as the tree trunk solid volume fraction and vegetated length parameter change. Therefore, as the number of tree trunks increases the effect of drag force, in terms of drag coefficient increases. This brings about an idea to define the drag coefficient in a normalized form that will take into consideration the variable amount of tree trunks. For the assessment of the normalized drag coefficient C_{DN}, by considering the assumptions mentioned above, which is associated with the debris flow resistance due to rigid tree trunks, C_{DN} is proposed as below:

$$C_{DN} = C_D \times \eta \quad (34)$$

Where C_D is the drag coefficient for incoming flow velocity and η is the mean value of the correlation drag coefficient for each different tree trunk density.

There are several different methods to define the tree trunk drag coefficient for the group tree trunk model in which C_D is not the same as a single tree trunk and has typically been accessed to increase with tree trunk density (Nepf, 1999; Tanino and Nepf, 2008; Kothyari et al., 2009 and Stoesser et al., 2009). The drag force was equally distributed within the control volume among the different tree trunks to examine drag coefficients.

The graph in Figure 26 shows the variation of normalized drag coefficient C_{DN} with various row numbers, Nr, as was given in Eq. (30). The values of η and C_{DN} for the six different group model B are in the range of about 1.0-2.5 and 0.2-1.2 (Table 10).

The graph exhibits that C_{DN} increases with an increase of row numbers. As the C_{DN} approaches to its maximum level, it approaches to a constant value even if Nr values continue to increase. This could be due to the possibility that the debris flow became fully developed after a certain length of vegetation array. Since the number of rows taken in this work increased to 1, 3, 5, 8, 12, and 17 for each model, the number of rows does not increase sequentially by one. As a result, the graph is selected as a curve by applying an exponential pattern, but if all these experiments are reapplied one by one, the relationship might be drawn as two straight lines. Therefore, future studies should be performed to improve the derived relationship.

The nonlinear regression equation describing the change in normalized drag coefficient with respect to number of rows is given in Eq. 35 with mean square error (MSE) 0.03 and the standard error of the regression (S) 0.18. Eq. 35 is derived for describing the normalized drag coefficient valid for the simulation performed in this study.

$$C_{DN} = 1.2 - 1.44 \exp\left(-0.24 N_r\right) \tag{35}$$

Table 10: Results of C_D, η and C_{DN} with different solid volume fraction

	C_D	**η**	**C_{DN}**
(ψ) %	**Group model A**		
1	0.066	1.0	0.1
1.96	0.62	9.4	5.9
3.9	0.44	6.6	2.9
7.8	0.87	13.2	11.5
15.7	0.71	10.7	7.6
31.4	`1.24	18.8	23.3
N_r	**Group model B**		
1	0.20	1.00	0.2
3	0.26	1.32	0.3
5	0.39	1.96	0.8
8	0.49	2.46	1.2
12	0.49	2.49	1.2
17	0.49	2.49	1.2

The values of η for linear group model A are in the range of about 1 to 10.7 and for rectilinear group model A are in the range of 9.4 to 18.8 (Table 10). The graph in Figure 27 shows the variation of normalized drag coefficient C_{DN} with various solid volume fractions (ψ) for linear and rectilinear tree trunk models. The C_{DN} increases with increasing the number of tree trunks within a predefined area in both linear and rectilinear models. As illustrated in Figure 27, the increase in rectilinear models is more pronounced compared to the linear model.

The normalized logarithmic regression equations with regression error square (R^2) of 0.98 for linear and 0.89 for rectilinear models respectively are:

$$\boldsymbol{C_{DN} = 2.7\ ln(100\psi) - 0.16} \quad (36)$$

$$\boldsymbol{C_{DN} = 8.3\ ln(100\psi) + 5.9} \quad (37)$$

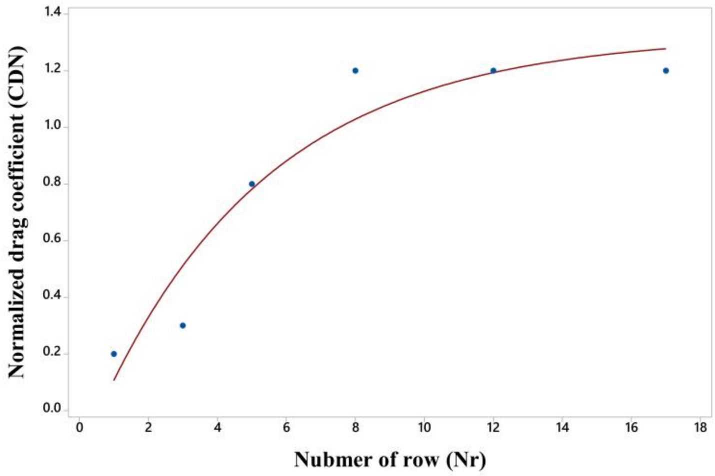

Figure 26:. Variation of normalized drag coefficient C_{DN} with various row numbers Nr for group model B

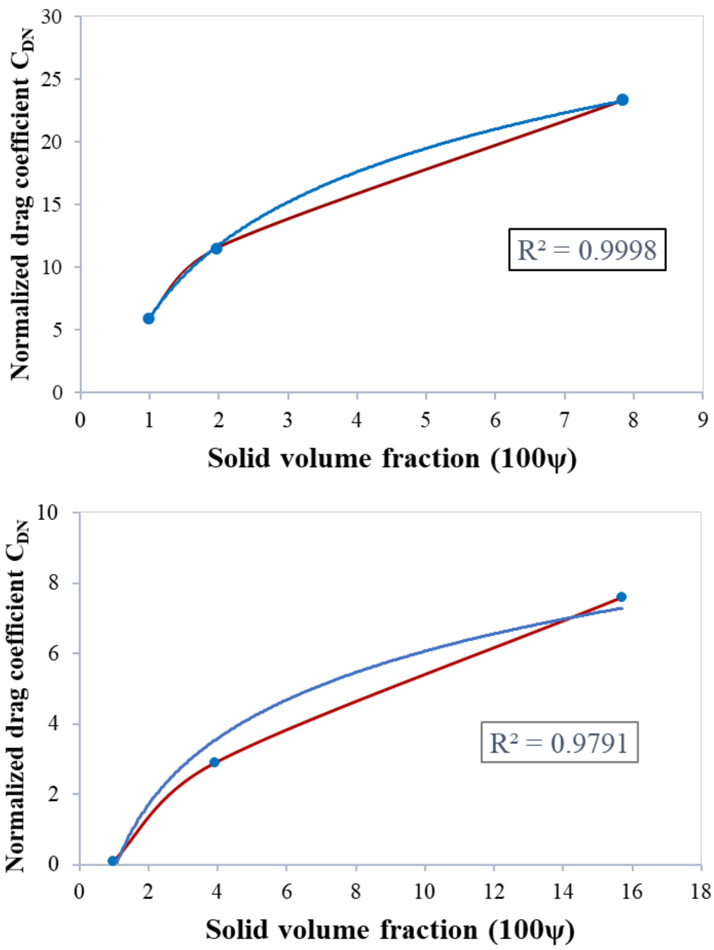

Figure 27: Variation of normalized drag coefficient C_{DN} with various solid volume fraction ψ for group model A (Linear and Rectilinear)

In order to assess more completely the influence of tree trunks on the C_D the normalized regression equation is defined as a function of Froude number and ψ for group model A and N_r for group mode B as follows:

$$C_{DN} = 39.69 - 0.33\ln(100\psi)^{0.002} - 30.38\ln(Fr)^{0.85} \quad (38)$$

$$C_{DN} = 7.45 - 0.12\ln(N_r)^{0.72} - 5.63\ln(Fr)^{0.99} \quad (39)$$

These equations imply that drag coefficients have a weak dependence on tree trunks solid volume fractions and row numbers when compared with the Froude number. According to the proposed equations and normalized drag coefficient estimated, C_{DN}, a satisfactorily agreement has been exhibited as shown in Figure 28.

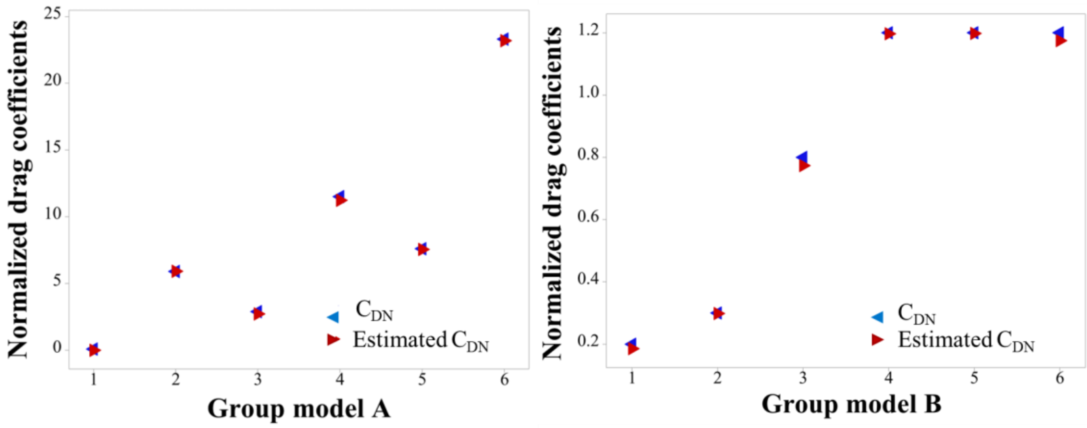

Figure 28: Comparison between the normalized drag coefficients C_{DN} and the estimated C_{DN} based on the results which obtained from Eq.38 and Eq.39 for both group models A and B.

Several factors affect the hydrodynamic empirical coefficient, for instance the characteristics of a basin, the features and properties of debris flows and intensity rainfall characteristics. Previously conducted the debris flow experimental results exhibit that the hydrodynamic empirical coefficient can be estimated within the range of (2.8–4.4) (Lichtenhahn, 1973), (2.5–7.5) (Scotton and Deganutti, 1997) and (0.45-2.2), (Armanini, 1997).

The hydrodynamic empirical coefficient (α) has been estimated experimentally by using a flume to evaluate the impact force of debris flow as explained above. Figure 29 depicts the variation of the dynamic empirical coefficient (α) as a function of the Froude number. In the present work, the presence of tree trunks increases the resistance forces, and the empirical coefficient is estimated to be in the range of (0.28–0.92) for the Froude number varying between 1.6 and 3.9. Referring to Eq. 3 by having a new finding of Pd_{max} the new regression hydrodynamic model with mean square error (MSE) 0.0004 and the standard error of the regression (S) 0.006 are introduced as:

$$\alpha = 0.15 F_r^{1.33} \tag{39}$$

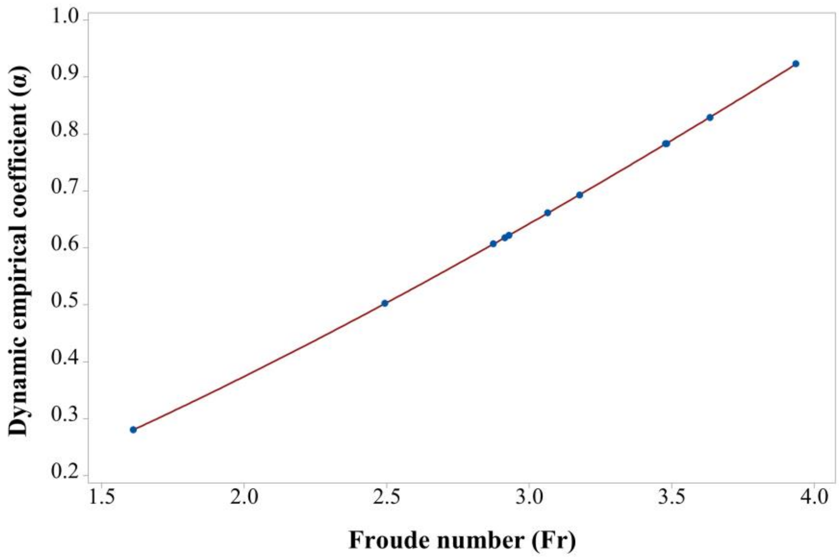

Figure 29: The correlation between the Froude number (Fr) and dynamic empirical coefficient, (α)

The values of (a) and (b) are determined for both group models A and B as 0.15 and 1.33, respectively. Therefore, the reduction in impact pressure due to the presence of the tree trunks decrease the magnitude of coefficient "a" and increase the magnitude of coefficient "b" when compared to the previous studies that were performed without mitigation methods.

Chapter 5

CONCLUSION

5.1 Discussion

Based on the analytical and numerical calculations, the ratio between pressure forces and inertia forces which is the dynamic empirical coefficient (α) has been modified for the cases where the protection of patch of tree trunks is present (Eq. 39). In this study, the values of (a) and (b) are determined as 0.15 and 1.33, respectively. As a result, the Froude number and dynamic empirical coefficient became linearly proportional to each other. However, under normal conditions (without any mitigation techniques) which have been studied previously, the value of (a) ranges from 4.9 to 5.62 and the value of (b) ranges from -1.66 to -1.29, indicating that the Froude number and (α) are inversely proportional (Hübl et al., 2009 and Cui et al., 2015).

This result depicts the effect of the patch of tree trunks on reducing the magnitude of inertia forces. Such reduction reduces the Froude number, therefore, in order to reduce (α) since inertia force (ρu^2) is decreasing Pd_{max} should also be decreased. This can only be satisfied if the constant (b) results in a positive value, 1.33. This result suggests that in the case of protective mitigation, the magnitude of (b) should be positive.

Implementation of baffle array is a similar artificial technique to mitigate debris flow disasters. Studies conducted by Bi et al., (2018); Wang et al., (2020) and Yang et al., (2021) demonstrated that the baffle row numbers, column spacing, and row spacing all have significant influences on the baffle energy dissipation. According to their results, increasing the number of baffle rows and spacing increases baffles energy dissipation capacity which indicates the reduction in the velocity of debris flow. Also, Ng et al., (2015) investigated the effects of baffle spacing and row numbers and their experimental results depicted reduced velocity by increasing row numbers of baffles. By increasing from one row to three rows, the velocity is reduced by 57 %. In this study, a reduction in the debris flow velocity is also observed. However, the reduction is not as high as in baffle cases but is up to 47% in the A type models and 21% for the B type models. Such a result indicates that natural mitigation methods might not be as successful as artificial ones but still can reduce risks generated by debris flow. In addition, Zhang et al., (2021) worked out the effect of baffle arrays at the acceleration-stage- of the granular-flow and according to their results, the velocity is reduced by 78.82%.

Many studies have recently investigated the drag coefficient exerted by cylindrical arrays in the case of water flow. These findings examined flow patterns similar to results investigated for debris flow in this study. Studies conducted by Tanino et al., (2008); tminan et al., (2017); Chang et al., (2020); Mancheño et al., (2021) and Sohrabi et al., (2023) showed that by increasing the solid volume fractions, the drag coefficient increases and consequently the drag force also increases. Also, D'Ippolito et al., (2019) investigated that by increasing the areal density the drag coefficient increases by 50 %. Since the density of the debris flow is higher than the water flow, the results of this study indicated the drag coefficient increases by 90% and 59% in both grope models A and B, respectively.

At the same time, some studies were done to examine the variation of exerted drag force with the effect of blockage and sheltering (Li and Shen, 1973; Schoneboom et al., 2011; Etminan et al., 2017 and Liu et al., 2020). From the perspective of the blockage and sheltering effect, our results also have been validated by those results. Etminan et al., (2017) and Liu et al., (2020) found that blockage effect with high vegetation densities had a greater impact on reducing drag coefficient than sheltering effects in rectilinear configurations. However, in the linear configurations with the constant blockage ratio, the sheltering effect showed more strength, which is evident that parallel findings regarding the blockage and sheltering effects have been observed in this study.

In this study, the rectilinear configurations of tree trunks in a designated area was more effective than other configurations. When the maximum impact pressures at A1 are compared with the maximum impact pressures at A6, a reduction of 67.3%, 69.5% and, 70% in maximum pressures are observed at S4, S3, and S2, respectively and a 34 % reduction in peak impact pressure for model B.

It can be seen that for group model A (linear and rectilinear), the maximum impact pressure concentration appears in a different region of the wall. The variation of impact pressure concentration is similar to the damaged regions of the wall. There is a relatively high impact pressure region over the wall from S1 to S4 in A1 (linear model). Increasing the tree trunk arrangements from A2 to A6 gradually reduces the effect of maximum impact pressure and expands its effect to a large area, therefore, the damaged regions are altered.

Future research should focus on studying the debris flow velocity field, with a particular concentration on the debris flow surfaces, and also, developing methods to determine the velocity field around patches of tree trunks.

In this study, it is assumed that the density remains constant throughout all simulation models and results, with the diameter of the tree trunk patches being uniform across all models. Additionally, the debris flow regime is assumed to be non-uniform and supercritical flow. A limitation of this study is that the models and results are primarily based on simulations, with limited field data for validation. This may affect the accuracy and applicability of the findings compared to real-world. Furthermore, external factors such as rainfall intensity, soil composition, and terrain variations are not accounted in this study.

5.2 Conclusion

The work reports focused on the effect of debris flow peak impact pressure on a vertical wall which has been analysed under the protection of a patch of tree trunks. Both numerical simulation and the analytical model have been applied and validated. Based on research findings, the following conclusions are drawn:

1) The numerical simulation results depicted that increasing the density of tree trunks within a designated area is 50% more protective than the increase in the number of rows of tree trunks.
2) Increase in the density is also effective in retarding the occurrence period of the peak flows in model A around 58%. For model B, since we only increased the number of rows, it has changed by 18.4% up to the B3 (five tree trunk rows) model and it has not affected on occurrence period of the peak for the other models at all. Thus, based on the results of the eight, twelve and seventeen rows

of tree trunks investigation, the design basis for the five rows of tree trunks is suggested for model B.

3) The maximum impact pressure is concentrated between 4.5 and 10.5 cm above the floor.
4) Based on the analytical calculations the drag coefficient has been developed as a function of the Froude number and the new dynamic empirical coefficient (α) has been modified based on the analytical results.
5) The drag coefficient is defined as a function of the vegetated length parameter and solid volume fractions.
6) The normalized regression equation of drag coefficient (C_D) is defined as a function of Froude number and ψ for group model A and a function of Froude number and N_r for group model B.

Accordingly, the presence of patches of tree trunks plays a significant role in reducing debris flow impact pressure and thus minimizing the hazard risks. It is clear that accurate numerical analysis and analytic methods can be effective in obtaining accurate debris flow impact force simulations. This study can be improved and developed by using different sediment and water concentrations to test the maximum impact pressure on walls. In addition, this study can be improved by using an experimental system, such as the physical model of the prototype, and converting the findings to values likely to be encountered in nature in future studies.

REFERENCES

Ahmadian, P., & Turker, U. Debris Flow Impact on Rigid Walls: Protection by Tree Trunks. *Turkish Journal of Civil Engineering, 35*(6).

Areas, N. R. C. (US). C. on M. for P. M. (1982). *Selecting a methodology for delineating mudslide hazard areas for the National Flood Insurance Program*. National Academies.

Armanini, A. (1997). On the dynamic impact of debris flows. In *Recent developments on debris flows* (pp. 208–226). Springer.

Armanini, A., Dellagiacoma, F., & Ferrari, L. (2005). From the check dam to the development of functional check dams. In *Fluvial hydraulics of mountain regions* (pp. 331–344). Springer.

Armanini, A., Rossi, G., & Larcher, M. (2019). Dynamic impact of a water and sediments surge against a rigid wall. *Journal of Hydraulic Research*.

Bagnold, R. A. (1954). Experiments on a gravity-free dispersion of large solid spheres in a Newtonian fluid under shear. *Proceedings of the Royal Society of London. Series A. Mathematical and Physical Sciences*, *225*(1160), 49–63.

Bel, C., Liébault, F., Navratil, O., Eckert, N., Bellot, H., Fontaine, F., & Laigle, D. (2017). Rainfall control of debris-flow triggering in the Réal Torrent, Southern French Prealps. *Geomorphology*, *291*, 17–32.

Bettella, F., Michelini, T., D'Agostino, V., & Bischetti, G. B. (2018). The ability of tree stems to intercept debris flows in forested fan areas: A laboratory modelling study. *Journal of Agricultural Engineering*, *49*(1), 42–51.

Bi, Y., Du, Y., He, S., Sun, X., Wang, D., Li, X., Liang, H., & Wu, Y. (2018). Numerical analysis of effect of baffle conFigure uration on impact force exerted from rock avalanches. *Landslides*, *15*(5), 1029–1043.

Booth, A. M., Sifford, C., Vascik, B., Siebert, C., & Buma, B. (2020). Large wood inhibits debris flow runout in forested southeast Alaska. *Earth Surface Processes and Landforms*, *45*(7), 1555–1568.

Chang, W.-Y., Constantinescu, G., & Tsai, W.-F. (2020). Effect of array submergence on flow and coherent structures through and around a circular array of rigid vertical cylinders. *Physics of Fluids*, *32*(3).

Choi, C. E., Ng, C. W. W., Law, R. P. H., Song, D., Kwan, J. S. H., & Ho, K. K. S. (2015). Computational investigation of baffle conFigure uration on impedance of channelized debris flow. *Canadian Geotechnical Journal*, *52*(2), 182–197.

Chu, T., Hill, G., McClung, D. M., Ngun, R., & Sherkat, R. (1995). Experiments on granular flows to predict avalanche runup. *Canadian Geotechnical Journal*, *32*(2), 285–295.

Costa, J. E. (1984). *Physical geomorphology of debris flows. In 'Developments and applications of geomorphology'.(Eds JE Costa, PJ Fleisher) pp. 268–317*.

Springer-Verlag: Berlin, Heidelberg.

Coussot, P., & Meunier, M. (1996). Recognition, classification and mechanical description of debris flows. *Earth-Science Reviews*, *40*(3–4), 209–227.

Cui, P., Zeng, C., & Lei, Y. (2015). Experimental analysis on the impact force of viscous debris flow. *Earth Surface Processes and Landforms*, *40*(12), 1644–1655.

D'Ippolito, A., Calomino, F., Alfonsi, G., & Lauria, A. (2021). Flow resistance in open channel due to vegetation at reach scale: A review. *Water*, *13*(2), 116.

D'Ippolito, A., Lauria, A., Alfonsi, G., & Calomino, F. (2019). Investigation of flow resistance exerted by rigid emergent vegetation in open channel. *Acta Geophysica*, *67*(3), 971–986.

Deng, J., & Kandel, P. (2022). Drag force on a circular cylinder in stratified flow: A two-dimensional numerical study. *Physics of Fluids*, *34*(5).

Egli, T. (2005). *Wegleitung Objektschutz gegen gravitative naturgefahren*. VKF.

Etminan, V., Lowe, R. J., & Ghisalberti, M. (2017). A new model for predicting the drag exerted by vegetation canopies. *Water Resources Research*, *53*(4), 3179–3196.

Fidej, G., Mikoš, M., Rugani, T., Jež, J., Kumelj, Š., & Diaci, J. (2015). Assessment of the protective function of forests against debris flows in a gorge of the Slovenian Alps. *IForest-Biogeosciences and Forestry*, *8*(1), 73.

Franco, A., Moernaut, J., Schneider-Muntau, B., Strasser, M., & Gems, B. (2021). Triggers and consequences of landslide-induced impulse waves–3D dynamic reconstruction of the Taan Fiord 2015 tsunami event. *Engineering Geology*, *294*, 106384.

Guilinger, J. (n.d.). *Debris Flow Types*. Retrieved April 2, 2024, from https://www.ppic.org/blog/whats-worse-than-a-flood-a-debris-flow/

He, J., Zhang, L., Fan, R., Zhou, S., Luo, H., & Peng, D. (2022). Evaluating effectiveness of mitigation measures for large debris flows in Wenchuan, China. *Landslides*, *19*(4), 913–928.

He, S., Liu, W., & Li, X. (2016). Prediction of impact force of debris flows based on distribution and size of particles. *Environmental Earth Sciences*, *75*(4), 298.

Hong, Y., Wang, J. P., Li, D. Q., Cao, Z. J., Ng, C. W. W., & Cui, P. (2015). Statistical and probabilistic analyses of impact pressure and discharge of debris flow from 139 events during 1961 and 2000 at Jiangjia Ravine, China. *Engineering Geology*, *187*, 122–134.

Hu, Y., Yu, Z., & Zhou, J. (2020). Numerical simulation of landslide-generated waves during the 11 October 2018 Baige landslide at the Jinsha River. *Landslides*, *17*(10), 2317–2328.

Huang, X., Zhang, Z., & Xiang, G. (2022). Sensitivity analysis of a built environment exposed to debris flow impacts with 3-D numerical simulations. *Natural Hazards Earth System Sci Discus*, *2022*, 1–27.

Huang, Y., & Zhang, B. (2022). Challenges and perspectives in designing engineering structures against debris-flow disaster. *European Journal of Environmental and Civil Engineering*, *26*(10), 4476–4497.

Hübl, J, & Holzinger, G. (2003). Development of design basis for crest open structures for debris flow management in torrents: miniaturized tests for the efficiency estimation of debris flow breakers. *WLS Report*, *50*.

Hübl, Johannes, Suda, J., Proske, D., Kaitna, R., & Scheidl, C. (2009). Debris flow impact estimation. *Proceedings of the 11th International Symposium on Water Management and Hydraulic Engineering, Ohrid, Macedonia*, *1*, 1–5.

Hungr, O, Morgan, G. C., & Kellerhals, R. (1984). Quantitative analysis of debris torrent hazards for design of remedial measures. *Canadian Geotechnical Journal*, *21*(4), 663–677.

Hungr, Oldrich. (2000). Analysis of debris flow surges using the theory of uniformly progressive flow. *Earth Surface Processes and Landforms: The Journal of the British Geomorphological Research Group*, *25*(5), 483–495.

Hungr, Oldrich, Leroueil, S., & Picarelli, L. (2014). The Varnes classification of landslide types, an update. *Landslides*, *11*, 167–194.

Iverson, R. M. (1997). of Debris. *Review of Geophysics*, *35*(97), 245–296.

Iverson, R. M., George, D. L., & Logan, M. (2016). Debris flow runup on vertical barriers and adverse slopes. *Journal of Geophysical Research: Earth Surface*, *121*(12), 2333–2357.

Iverson, R. M., Logan, M., LaHusen, R. G., & Berti, M. (2010). The perfect debris flow? Aggregated results from 28 large-scale experiments. *Journal of Geophysical Research: Earth Surface*, *115*(F3).

Iverson, R. M., & Ouyang, C. (2015). Entrainment of bed material by Earth-surface mass flows: Review and reformulation of depth-integrated theory. *Reviews of Geophysics*, *53*(1), 27–58.

Jakob, M., Hungr, O., & Jakob, D. M. (2005). *Debris-flow hazards and related phenomena* (Vol. 739). Springer.

Julien, P. Y., & Leon, C. (2000). Mud floods, mudflows and debris flows. Classification, rheology and structural design. *Jornadas de Investigación JIFI*.

Kaitna, R., Palucis, M. C., Yohannes, B., Hill, K. M., & Dietrich, W. E. (2016). Effects of coarse grain size distribution and fine particle content on pore fluid pressure and shear behavior in experimental debris flows. *Journal of Geophysical Research: Earth Surface*, *121*(2), 415–441.

Kang, T., Jang, C.-L., Kimura, I., & Lee, N. (2022). Numerical Simulation of Debris

Flow and Driftwood with Entrainment of Sediment. *Water*, *14*(22), 3673.

Khonkaen, P., & Cheng, J.-D. (2011). The application of check dams construction to watershed management: a case study in the North of Thailand. *Journal of Soil and Water Conservation*, *43*(1), 111–122.

Kim, B.-J., Choi, C. E., & Yune, C.-Y. (2023). Multi-scale flume investigation of the influence of cylindrical baffles on the mobility of landslide debris. *Engineering Geology*, *314*, 107012.

Kim, B.-J., & Yune, C.-Y. (2022). Flume investigation of cylindrical baffles on landslide debris energy dissipation. *Landslides*, *19*(12), 3043–3060.

Kim, S. J., & Stoesser, T. (2011). Closure modeling and direct simulation of vegetation drag in flow through emergent vegetation. *Water Resources Research*, *47*(10).

Kothyari, U. C., Hayashi, K., & Hashimoto, H. (2009). Drag coefficient of unsubmerged rigid vegetation stems in open channel flows. *Journal of Hydraulic Research*, *47*(6), 691–699.

Kumar, R., & Singh, N. K. (2021). Three dimensional flow over elliptic cylinders arrays in octagonal arrangement. *Journal of Thermal Engineering*, *7*(Supp 14), 2031–2040.

Lei, Y., Cui, P., Zeng, C., & Guo, Y. (2018). An empirical mode decomposition-based signal process method for two-phase debris flow impact. *Landslides*, *15*(2), 297–

307.

Leonardi, A., & Pirulli, M. (2020). Analysis of the load exerted by debris flows on filter barriers: Comparison between numerical results and field measurements. *Computers and Geotechnics*, *118*, 103311.

Li, R.-M., & Shen, H. W. (1973). Effect of tall vegetations on flow and sediment. *Journal of the Hydraulics Division*, *99*(5), 793–814.

Li, Xiangbo, Fu, J., Chen, Q., Liu, X., & Liu, H. (2011). The Concept of Sandy Debris Flow and Its Application in the Yanchang Formation Deep Water Sedimentation of the Ordos Basin□□. *Advances in Earth Science*, *26*(3), 286.

Li, Xinpo, Yan, Q., Zhao, S., Luo, Y., Wu, Y., & Wang, D. (2020). Investigation of influence of baffles on landslide debris mobility by 3D material point method. *Landslides*, *17*, 1129–1143.

Lichtenhahn, C. (1973). Berechnung von sperren in beton und eisenbeton. *Mitt Forstl Bundes Versuchsanst Wein*.

Liu, C., & Nepf, H. (2016). Sediment deposition within and around a finite patch of model vegetation over a range of channel velocity. *Water Resources Research*, *52*(1), 600–612.

Liu, M.-Y., Huai, W.-X., Yang, Z.-H., & Zeng, Y.-H. (2020). A genetic programming-based model for drag coefficient of emergent vegetation in open channel flows.

Advances in Water Resources, *140*, 103582.

Liu, W., Yang, Z., & He, S. (2021). Modeling the landslide-generated debris flow from formation to propagation and run-out by considering the effect of vegetation. *Landslides*, *18*, 43–58.

Lo, D. O. K. (2000). *Review of natural terrain landslide debris-resisting barrier design*. Geotechnical Engineering Office, Civil Engineering Department.

Lorenzo MARCHI. (n.d.). *Debris Flow Types*. Retrieved April 1, 2024, from https://www.irpi.cnr.it/en/focus/debris-flow-monitoring/

Mahnamfar, F., Abdollahzadehmoradi, y., & Ağiralioğlu, n. (2020). Flood risk analysis of residential areas at downstream side of Elmali Dam. *Academic Platform Journal of Natural Hazards and Disaster Management*, *1*(1), 49–58.

Malvern, L. E. (1969). *Introduction to the Mechanics of a Continuous Medium* (Issue Monograph).

Mancheño, A. G., Jansen, W., Uijttewaal, W. S. J., Reniers, A., van Rooijen, A. A., Suzuki, T., Etminan, V., & Winterwerp, J. C. (2021). Wave transmission and drag coefficients through dense cylinder arrays: Implications for designing structures for mangrove restoration. *Ecological Engineering*, *165*, 106231.

Mangeney, A., Roche, O., Hungr, O., Mangold, N., Faccanoni, G., & Lucas, A. (2010). Erosion and mobility in granular collapse over sloping beds. *Journal of*

Geophysical Research: Earth Surface, *115*(F3).

Mashud, M., Al-Bari, A., & Kader, M. G. (2011). Experimental investigation of drag force reduction mechanism for flow around a circular cylinder. *International Journal of Engineering and Applied Sciences*, *3*(2), 69–75.

Nakagawa, H., Satofuka, Y., & Takahama, J. (2002). Water Induced Hazard–I. Sub Text Book, M. Sc. *Water Resources Engineering, Institute of Engineering, Tribhuvan University, Nepal*.

Nepf, H. M. (1999). Drag, turbulence, and diffusion in flow through emergent vegetation. *Water Resources Research*, *35*(2), 479–489.

Nepf, H. M. (2012). Hydrodynamics of vegetated channels. *Journal of Hydraulic Research*, *50*(3), 262–279.

Ng, C. W. W., Choi, C. E., Song, D., Kwan, J. H. S., Koo, R. C. H., Shiu, H. Y. K., & Ho, K. K. S. (2015a). Physical modeling of baffles influence on landslide debris mobility: Baffle physical modeling influence on landslide debris mobility. *Landslides*, *12*, 1–18.

Ng, C. W. W., Choi, C. E., Song, D., Kwan, J. H. S., Koo, R. C. H., Shiu, H. Y. K., & Ho, K. K. S. (2015b). Physical modeling of baffles influence on landslide debris mobility. *Landslides*, *12*(1), 1–18.

Ng, C. W. W., Song, D., Choi, C. E., Liu, L. H. D., Kwan, J. S. H., Koo, R. C. H., &

Pun, W. K. (2017). Impact mechanisms of granular and viscous flows on rigid and flexible barriers. *Canadian Geotechnical Journal*, *54*(2), 188–206.

Passive Method, Vegetative barriers. (n.d.). Retrieved January 9, 2024, from https://vetiversenegal.blogspot.com/2014/04/le-systeme-vetiver-une-solution-pour-le.html

Remaître, A., & Malet, J. P. (2010). The effectiveness of torrent check dams to control channel instability: example of debris-flow events in clay shales. *Check Dams, Morphological Adjustements and Erosion Control in Torrential Streams, Edited by: Garcia, CC and Lenzi, MA, Nova Science Publishers Inc., New York*, 211–237.

Riazi, A., & Türker, U. (2019). The drag coefficient and settling velocity of natural sediment particles. *Computational Particle Mechanics*, *6*(3), 427–437.

Scheidl, C., Chiari, M., Mullegger, M., & Proske, D. (2012). Estimation of debris-flow impact forces using a small scale modelling approach. *12th Congress Interpraevent*.

Schoneboom, T., Aberle, J., & Dittrich, A. (2011). Spatial variability, mean drag forces, and drag coefficients in an array of rigid cylinders. *Experimental Methods in Hydraulic Research*, 255–265.

Scotten, P., & Trivellato, F. (1995). Dynamic pressure on check-dam due to debris flow collision. *Proceedings of Twelfth Australasian Fluid Mechanics*

Conference, Online: Http://People. Eng. Unimelb. Edu. Au/Imarusic/Proceedings/12/Scotton. Pdf, *15*, 2014.

Scotton, P., & Deganutti, A. M. (1997). Phreatic line and dynamic impact in laboratory debris flow experiments. *Debris-Flow Hazards Mitigation: Mechanics, Prediction, and Assessment*, 777–786.

Sediment Control Practices. (n.d.). Retrieved February 9, 2024, from https://stormwater.pca.state.mn.us/index.php?title=Sediment_control_practices_-_Sediment_traps_and_basins

Shrestha, B. B., Nakagawa, H., Kawaike, K., & BABA, Y. (2008). Numerical and experimental study on debris-flow deposition and erosion upstream of a check dam. *Proceedings of Hydraulic Engineering*, *52*, 139–144.

Sohrabi, S., Afzalimehr, H., & Singh, V. P. (2023). Estimation of drag coefficient of emergent and submerged vegetation patches with various densities and arrangements in open channel flow. *ISH Journal of Hydraulic Engineering*, *29*(3), 297–307.

Song, D., Chen, X., Zhou, G. G. D., Lu, X., Cheng, G., & Chen, Q. (2021). Impact dynamics of debris flow against rigid obstacle in laboratory experiments. *Engineering Geology*, *291*, 106211.

Stoesser, T., Salvador, G. P., Rodi, W., & Diplas, P. (2009). Large eddy simulation of turbulent flow through submerged vegetation. *Transport in Porous Media*, *78*(3), 347–365.

Takahashi, T. (1979). Study of the deposition of debris flows (1)-deposition due to abrupt change of bed slope-. *Ann. Disaster Prevention Res. Inst. Kyoto Univ., 22*, 315–328.

Takahashi, T. (2014). *Debris Flow: Mechanics, Prediction and Countermeasures, 2nd edition. CRC Press*.

Tang, J., & Hu, K. (2018). A debris-flow impact pressure model combining material characteristics and flow dynamic parameters. *Journal of Mountain Science, 15*(12), 2721–2729.

Tanino, Y., & Nepf, H. M. (2008). Laboratory investigation of mean drag in a random array of rigid, emergent cylinders. *Journal of Hydraulic Engineering*, *134*(1), 34–41.

Thouret, J.-C., Antoine, S., Magill, C., & Ollier, C. (2020). Lahars and debris flows: Characteristics and impacts. *Earth-Science Reviews, 201*, 103003.

Tiberghien, D., Laigle, D., Naaim, M., Thibert, E., & Ousset, F. (2007). Experimental investigations of interaction between mudflow and an obstacle. *Debris-Flow Hazards Mitigation: Mechanics, Prediction and Assessment, Millpress, Rotterdam*.

Türker, U, Yagci, O., & Kabdaşlı, M. S. (2006). Analysis of coastal damage of a beach profile under the protection of emergent vegetation. *Ocean Engineering*, *33*(5–6), 810–828.

Türker, Umut, & Valyrakis, M. (2021). Hydraulic jump on rough beds: conceptual modeling and experimental validation. *Water Supply*, *21*(4), 1423–1437.

Türker, Umut, Yagci, O., & Kabdasli, M. S. (2019). Impact of nearshore vegetation on coastal dune erosion: assessment through laboratory experiments. *Environmental Earth Sciences*, *78*(19), 1–14.

Valyrakis, M., Liu, D., Turker, U., & Yagci, O. (2021). The role of increasing riverbank vegetation density on flow dynamics across an asymmetrical channel. *Environmental Fluid Mechanics, 21,* 643–666.

Vargas-Luna, A., Crosato, A., & Uijttewaal, W. S. J. (2015). Effects of vegetation on flow and sediment transport: comparative analyses and validation of predicting models. *Earth Surface Processes and Landforms*, *40*(2), 157–176.

Wang, B., Li, Y., Liu, D., & Liu, J. (2018). Debris flow density determined by grain composition. *Landslides, 15,* 1205–1213.

Wang, D., Li, Q., Bi, Y., & He, S. (2020). Effects of new baffles system under the impact of rock avalanches. *Engineering Geology, 264,* 105261.

Watanabe, M. (1981). *Investigation and Analysis of Volcanic Mud Flows in Mt sakurajima, Japan*.

Wilford, D. J., Sakals, M. E., Innes, J. L., & Sidle, R. C. (2005). *Fans with forests: contemporary hydrogeomorphic processes on fans with forests in west central British Columbia, Canada*.

Wilson, C., Stoesser, T., Bates, P. D., & Pinzen, A. B. (2003). Open channel flow through different forms of submerged flexible vegetation. *Journal of Hydraulic Engineering*, *129*(11), 847–853.

Xiong, Z., Chen, X.-Q., & Chen, J.-G. (2023). Control and Interception Characteristics of the Debris-Flow Flexible Net Barrier Based on Orthogonal Design. *Water*, *15*(10), 1809.

Yan, Y., Tang, H., Hu, K., Turowski, J. M., & Wei, F. (2023). Deriving Debris-Flow Dynamics From Real-Time Impact-Force Measurements. *Journal of Geophysical Research: Earth Surface*, *128*(3), e2022JF006715.

Yang, E., Bui, H. H., Nguyen, G. D., Choi, C. E., Ng, C. W. W., De Sterck, H., & Bouazza, A. (2021). Numerical investigation of the mechanism of granular flow impact on rigid control structures. *Acta Geotechnica*, *16*(8), 2505–2527.

Yazid, A. S., Adnan, T. F. F. T., Abdullah, A. A., Daud, W. N. W., Salleh, F., & Husin, M. R. (2017). Flood risk mitigation: Pressing issues and challenges. *International Review of Management and Marketing*, *7*(1), 157–163.

Zanchetta, G., Sulpizio, R., Pareschi, M. T., Leoni, F. M., & Santacroce, R. (2004). Characteristics of May 5–6, 1998 volcaniclastic debris flows in the Sarno area

(Campania, southern Italy): relationships to structural damage and hazard zonation. *Journal of Volcanology and Geothermal Research*, *133*(1–4), 377–393.

Zhang, B., Huang, Y., & Liu, J. (2021). Micro-mechanism and efficiency of baffle structure in deceleration of granular flows. *Acta Geotechnica*, *16*(11), 3667–3688.

Zhang, S. (1993). A comprehensive approach to the observation and prevention of debris flows in China. *Natural Hazards*, *7*(1), 1–23.

Zhang, S., & Yuan, J. (1985). Impact force of debris flow and its detection. *Memoirs of Lanzhou Institute of Glaciology and Cryopedology, Chinese Academy of Sciences. Beijing: Science Press*, 269–274.

Zhang, Y., Chen, J., Tan, C., Bao, Y., Han, X., Yan, J., & Mehmood, Q. (2021). A novel approach to simulating debris flow runout via a three-dimensional CFD code: a case study of Xiaojia Gully. *Bulletin of Engineering Geology and the Environment*, *80*(7), 5293–5313.

APPENDIX

Determine the Optimal Mesh Configurations in FLOW-3D

Using an excessively fine mesh increases the number of elements and equations the software needs to solve, which significantly slows down the simulation and consumes more computational resources (memory, CPU time). In this study, several mesh independence tests are performed in the simulation model by running simulations with varying mesh densities to ensure the results stabilize and do not change significantly with finer meshes. For the simulation model without tree trunk patches, six different runs are performed to achieve the point where the impact pressure are reliable and will not change with further refinement as indicated in below Figure. As a result, the peak impact pressure for the model without tree trunk patches was calculated to be 31.9 (kPa).

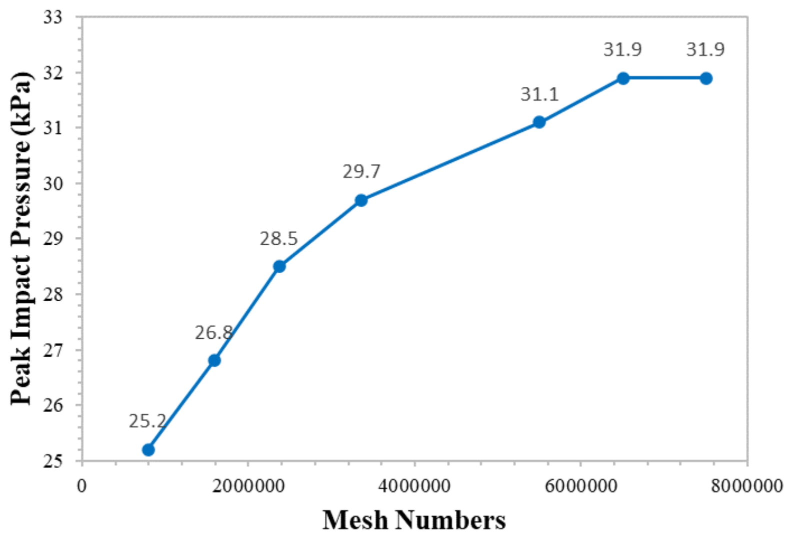

Similarly, for the simulation model with tree trunk patches, six different runs were conducted to reach a point where the impact pressure became stable and did not vary with further refinement. As shown in the Figure below, the peak impact pressure was determined to be 44.3 (kPa).

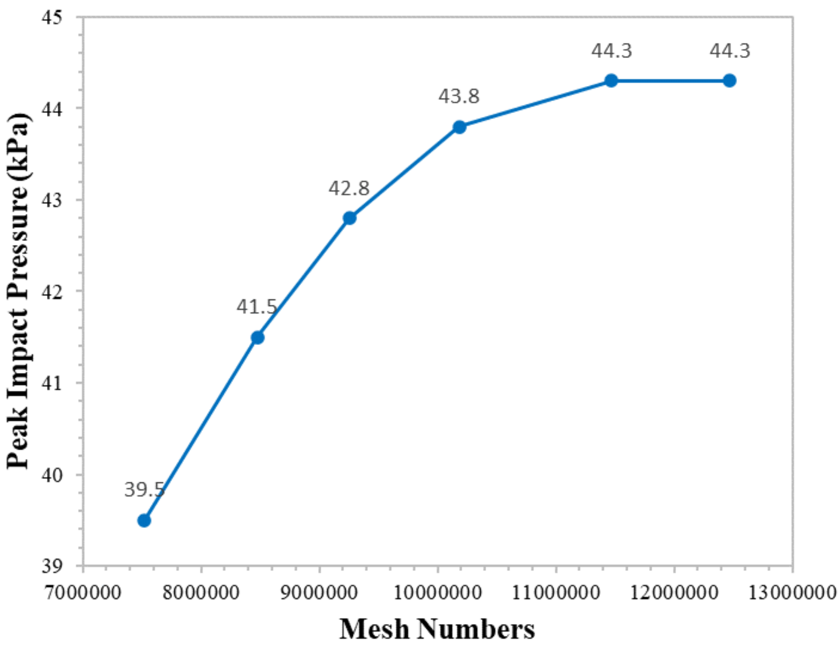
45
44
43
42
41
40
39
44.3
44.3
43.8
42.8
41.5
39.5
Peak Impact Pressure (kPa)
7000000
8000000
9000000
10000000
11000000
12000000
13000000
Mesh Numbers